Overview of the Microscopic Imager Investigation during Spirit's first 450 sols in Gusev crater

Ken E. Herkenhoff,[1] Steve W. Squyres,[2] Robert Anderson,[3] Brent A. Archinal,[1] Raymond E. Arvidson,[4] Janet M. Barrett,[1] Kris J. Becker,[1] James F. Bell III,[2] Charles Budney,[3] Nathalie A. Cabrol,[5] Mary G. Chapman,[1] Debbie Cook,[1] Bethany L. Ehlmann,[6] Jack Farmer,[7] Brenda Franklin,[3] Lisa R. Gaddis,[1] Donna M. Galuszka,[1] Patricia A. Garcia,[1] Trent M. Hare,[1] Elpitha Howington-Kraus,[1] Jeffrey R. Johnson,[1] Sarah Johnson,[8] Kjartan Kinch,[2] Randolph L. Kirk,[1] Ella Mae Lee,[1] Craig Leff,[3] Mark Lemmon,[9] Morten B. Madsen,[10] Justin N. Maki,[3] Kevin F. Mullins,[1] Bonnie L. Redding,[1] Lutz Richter,[11] Mark R. Rosiek,[1] Michael H. Sims,[12] Laurence A. Soderblom,[1] Nicole Spanovich,[13] Richard Springer,[3] Robert M. Sucharski,[1] Tracie Sucharski,[1] Rob Sullivan,[2] James M. Torson,[1] and Albert Yen[3]

Received 30 August 2005; revised 21 October 2005; accepted 3 November 2005; published 16 February 2006.

[1] The Microscopic Imager (MI) on the Mars Exploration Rover Spirit has returned images of Mars with higher resolution than any previous camera system, allowing detailed petrographic and sedimentological studies of the rocks and soils at the Gusev landing site. Designed to simulate a geologist's hand lens, the MI is mounted on Spirit's instrument arm and can resolve objects 0.1 mm in size or larger. This paper provides an overview of MI operations, data calibration, processing, and analysis of MI data returned during the first 450 sols (Mars days) of the Spirit landed mission. The primary goal of this paper is to facilitate further analyses of MI data by summarizing the methods used to acquire and process the data, the radiometric and geometric accuracy of MI data products, and the availability of archival products. In addition, scientific results of the MI investigation are summarized. MI observations show that poorly sorted soils are common in Gusev crater, although aeolian bedforms have well-sorted coarse sand grains on their surfaces. Abraded surfaces of plains rocks show igneous textures, light-toned veins or fracture-filling minerals, and discrete coatings. The rocks in the Columbia Hills have a wide variety of granular textures, consistent with volcaniclastic or impact origins. Case hardening and submillimeter veins observed in the rocks as well as soil crusts and cemented clods imply episodic subsurface aqueous fluid movement, which has altered multiple geologic units in the Columbia Hills. The MI also monitored Spirit's solar panels and the magnets on the rover's deck.

Citation: Herkenhoff, K. E., et al. (2006), Overview of the Microscopic Imager Investigation during Spirit's first 450 sols in Gusev crater, *J. Geophys. Res.*, *111*, E02S04, doi:10.1029/2005JE002574.

[1]Astrogeology Team, U.S. Geological Survey, Flagstaff, Arizona, USA.
[2]Department of Astronomy, Space Sciences Building, Cornell University, Ithaca, New York, USA.
[3]Jet Propulsion Laboratory, California Institute of Technology, Pasadena, California, USA.
[4]Department of Earth and Planetary Sciences, Washington University, St. Louis, Missouri, USA.
[5]NASA Ames Research Center/SETI Institute, Moffett Field, California, USA.
[6]Environmental Change Institute, Department of Geography and Environment, University of Oxford, Oxford, UK.
[7]Department of Geological Sciences, Arizona State University, Tempe, Arizona, USA.
[8]Department of Earth, Atmospheric and Planetary Sciences, Massachusetts Institute of Technology, Cambridge, Massachusetts, USA.
[9]Department of Atmospheric Sciences, Texas A&M University, College Station, Texas, USA.
[10]Center for Planetary Science, Danish Space Research Institute and Niels Bohr Institute for Astronomy, Physics and Geophysics, University of Copenhagen, Copenhagen, Denmark.
[11]DLR Institut für Raumsimulation, Cologne, Germany.
[12]NASA Ames Research Center, Moffett Field, California, USA.
[13]Lunar and Planetary Laboratory, University of Arizona, Tucson, Arizona, USA.

0148-0227/06/2005JE002574$09.00

1. Introduction

[2] The Mars Exploration Rover (MER) mission includes two essentially identical rovers, Spirit and Opportunity [*Crisp et al.*, 2003]. The Athena science payload [*Squyres et al.*, 2003] on each rover includes a Microscopic Imager. The Microscopic Imager (MI) is a fixed-focus camera mounted on a mechanical arm called the Instrument Deployment Device (IDD). The MI includes the same charge-coupled device (CCD) detector and electronics as the other MER cameras [*Bell et al.*, 2003; *Maki et al.*, 2003]. MI images are 1024 × 1024 pixels in size, with a scale of 31 microns/pixel at best focus. The MI optics are protected by a retractable Kapton dust cover. The instrument includes a contact sensor that is used to accurately position the MI relative to rock targets (Figure 1). Details of the camera design have been published previously [*Herkenhoff et al.*, 2003].

[3] This paper provides an overview of Spirit MI operations, calibration, processing and analyses of data acquired through Sol 450, during the first Earth year of landed operations (a sol is a Martian day, approximately 24 hours and 40 minutes long). Preliminary scientific results of the primary mission (through Sol 90) were described previously [*Squyres et al.*, 2004; *Greeley et al.*, 2004; *Arvidson et al.*, 2004; *Herkenhoff et al.*, 2004b; *McSween et al.*, 2004; *Bell et al.*, 2004; *Bertelsen et al.*, 2004; *Grant et al.*, 2004], so this paper focuses on the reduction and analysis of MI data acquired from Sol 91 to 450. *Arvidson et al.* [2006] provide an overview of the mission from landing to rover traverses and measurements in the Columbia Hills (starting on Sol 157), with a summary of key scientific findings. During the first 450 sols of the surface mission, the Spirit rover acquired and returned 2050 full-frame MI images.

2. MI Tactical Operations

[4] MER surface operations are conducted by a team of scientists and engineers for each rover [*Arvidson et al.*, 2006]. Each day, two MI personnel are assigned to each rover: an MI Payload Uplink Lead (PUL) and an MI Payload Downlink Lead (PDL). Early in the Spirit mission, the entire MER operations team worked 7 days a week at the Jet Propulsion Laboratory (JPL) in Pasadena, California, on schedules tied to the Martian day (''Mars time''). Because the Martian day (or ''sol'') is about 40 minutes longer than an Earth day, work shifts cycled through all times of the Earth day or night. At the end of Spirit's primary mission, MER operations transitioned to a more sustainable ''Earth time'' schedule in which the operations work was constrained to be during the Earth day. Details of MI uplink (Earth to Spirit) and downlink (Spirit to Earth) operations are described below.

2.1. Uplink

[5] At the beginning of the uplink process, MI observation requests are presented to the MER Science Operations Working Group (SOWG). If these requests are approved, the MI PUL generates the necessary command sequences and delivers them to the rover Sequence Integration Engineer for subsequent spacecraft uplink. As part of this process, MI targets of interest are communicated to IDD operations personnel, who characterize and validate the MI target positions using a three-dimensional terrain model derived from Front Hazcam (hazard avoidance cameras [see *Maki et al.*, 2003]) stereo images. The MI PUL is responsible for selecting MI command parameters such as exposure, dust cover state, data compression, number of images and the downlink priorities, all in conformance with the approved SOWG activity plan. Heating of the MI electronics, if necessary to bring the temperature into operating range (−55°C to 5°C), is commanded by the tactical engineering team.

[6] Most MI images of Mars are acquired using the autoexposure capabilities of the MER flight software [*Maki et al.*, 2003]. Because it is difficult to predict accurately how MI targets will be illuminated, autoexposure parameters are set to avoid saturation yet maintain reasonable signal/noise. However, specular reflections from some areas of the target sometimes cause saturation (4095 DN) and blooming. As in all the MER cameras, blooming results when excess charge spills out of a pixel into adjacent pixels [*Herkenhoff et al.*, 2003].

[7] The MI's fixed focus and 3 mm depth of field require that data be acquired as stacks of images at 3 mm intervals normal to the average surface plane to ensure acquisition of in-focus data. Smooth, flat surfaces that have been contacted by the Mössbauer spectrometer [*Klingelhöfer et al.*, 2003] or MI contact sensors usually require 3 images whereas rougher surfaces such as soil and high-relief rock faces require 5 to 7 images to assure focus throughout the field of view. Stereo coverage is acquired by taking an image offset (typically) 15 mm laterally at the predicted best focus position, usually at the level of the center of an image stack.

[8] The millimeter-scale movement of the MI is accomplished by the Rover Planners, who are responsible for commanding the rover's IDD. Precise location of the target surface with respect to the rover and the IDD is crucial, both for acquiring useful data and for assuring safety of the instrument and spacecraft. Depending on conditions, several methods yield accurate target surface location in three-dimensional space. Feedback from surface contact sensing is usually most reliable. A desired target is located within a Front Hazcam image with gross ranging information provided by stereo image data. A relatively flat and solid surface can then be safely touched by the MI contact sensor, which is aligned parallel to the boresight, outside the MI field of view (Figure 1). The tip of the probe is 44 mm in front of the MI optics with a 2 mm stroke, yielding an accurate distance from the camera to the target surface. Exact position feedback subsequently allows the Rover Planner to place the IDD and MI precisely, acquiring the desired images without endangering the instrument. Very high-relief rock surfaces and soft soils are more successfully located by touching with the Mössbauer faceplate (the MI probe could slip through a soft soil or dust surface or deep into a rock cavity without detecting resistance, possibly contaminating or damaging the instrument). The Mössbauer contact sensor detects the surface when the resistance limit (∼1 N) is exceeded.

[9] The MI optics are protected from dust contamination by a cover that includes a Kapton polyimide window, usually commanded to the open position during MI imaging

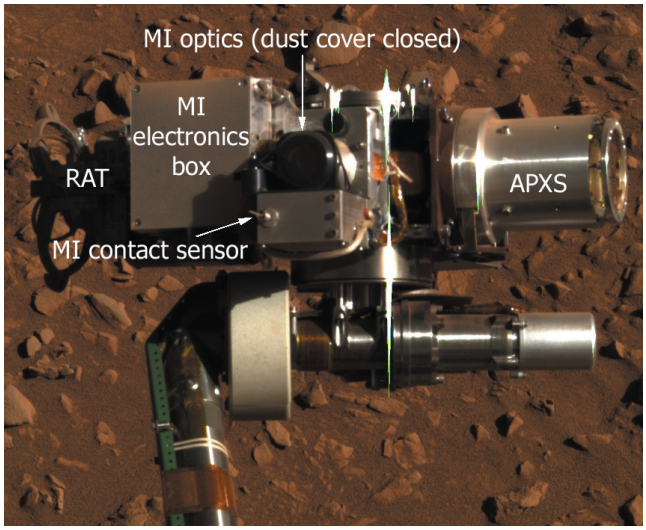

Figure 1. Pancam color (filters L4, L5, and L6) image of Spirit's IDD turret, taken on Sol 287. Bright vertical lines right of center are artifacts caused by blooming of saturated pixels. Illumination from upper right; turret is about 30 cm across.

activities. The protection is particularly important because the MI's placement at the end of the IDD along with the other instruments requires it to be articulated through space, including pointing toward the sky, depending on IDD instrument package activities. Occasionally the cover is left in place (closed) and images are taken through it to generate crude color information (e.g., Figure 23). The dust cover window is tinted orange, and shifts the effective wavelength of the MI about 12 nm toward the red [*Herkenhoff et al.*, 2003]. As dust accumulated on the MI dust cover, images taken through it showed decreased contrast, and the usefulness of MI color composites was reduced. Therefore very few MI images were taken through the dust cover during the extended mission.

[10] The MI PUL must understand overall energy, data volume and time constraints on the planned activities for the sol and judge how the MI requests can best be implemented. For instance, a typical MI mosaic requested after the Rock Abrasion Tool (RAT) [*Gorevan et al.*, 2003] grinds into a rock (i.e., creates a "RAT hole") is a 2 × 2 set of MI images, including stereo, covering the abraded target. The mosaic consists of two rows and two columns of 5 images per stack, plus one offset stereo image for each stack. Using lossless compression, the total data volume of the 24 images is typically 125 Mbits, whereas lossy compression can be used to reduce the data volume significantly. The volume of products generated by MI mosaics is constrained by the predictions of power availability, available on-board memory, number of data products stored, and volume of downlink (typically between 50 and 200 Mbits/day). MI activities must be prioritized relative to other engineering and science data requests in the same activity plan. Science and engineering teams balance all the factors in the planning process, generating guideline compression and downlink priorities for the requested MI data products. During the sequencing process, the MI PUL may be required to adjust compression and downlink priorities to fit engineering restrictions as they become more accurately known during the daily tactical process. Typically, the predicted best focus image from each stack in a mosaic has its downlink priority set at a relatively high level, while the balance of the data products, less likely to be in good focus, are returned at a lower downlink priority. The images returned to Earth first are then used to determine whether any of the images stored onboard the rover are likely out of focus. If rover memory is tightly constrained, the lower priority, poorly focused images can be deleted rather than returned to Earth. Thumbnail versions of all images are typically returned on the sol they are acquired to quickly confirm that images were successfully acquired, but are not useful for determining how well focused the images are.

[11] MI PUL responsibilities also include sequencing the six engineering cameras, which are used for driving, localization, assessing IDD reachability and targets, and documentation of various spacecraft and instrument conditions. Virtually all MI observations are documented via a corresponding stereo pair of Hazcam images showing the deployed IDD. Overall MER uplink planning is described by *Arvidson et al.* [2006].

[12] At the beginning of the second extended mission (October 2004), we began operating the MI and engineering cameras on Opportunity mostly from remote locations. Meanwhile, Spirit MI and engineering camera uplink operations have largely been conducted at JPL, with occasional remote PUL work. This has allowed each PUL to focus primarily on the operation of the cameras on one rover. The locations for remote MI PUL activities have included the U.S. Geological Survey (USGS) in Flagstaff, the NASA Ames Research Center, the University of Arizona, and Cornell University. By using video- and tele-conferencing and network tools, remote operations for practical purposes have become almost equivalent to operations at JPL. The primary activities of the remote PUL are (1) make recommendations and advise the science planning process, (2) verify validity of final science plans, (3) develop and/or verify image acquisition plan with rover planner, (4) develop new imaging sequences as necessary, (5) deliver all MI and engineering cameras sequences, (6) store all sequences in the permanent repositories, and (7) finish record keeping and reports for permanent record of sol's activities.

[13] Task (1) is typically accomplished via email, video- and tele-conferencing. Task (2) is accomplished via remote use of the MER planning software system, and although sometimes cumbersome, it is viable. Task (3) is done by voice conversations typically over a teleconference line. Task (4) is done either by remote login into JPL or by using a locally installed sequence development program. Tasks (5), (6) and (7) are facilitated by a number of software tools for delivery and reports generation. If care is taken in the operations design then modern communication systems make remote uplink operations an acceptably efficient and convenient process.

2.2. Downlink

[14] Most MI images are acquired and processed onboard Spirit using the MER onboard image processing capabilities [*Maki et al.*, 2003]. After acquiring the raw image using an autoexposure algorithm, a zero-second "shutter" image is

automatically subtracted from the raw image and the resulting image is scaled from 12 to 8 bits using an onboard lookup table [*Bell et al.*, 2006]. Although the capability exists to perform image subframing, it has been rarely used on MI images. The images are then compressed (lossy or losslessly) and stored in rover memory for later downlink. A full-size MI image, 1024 columns × 1024 rows, yields 1,048,576 pixels. The lowest compression rate, yielding the largest data products, is lossless. The highest compression rate, $^1/_4$ bit per pixel, yields the smallest data product and is usually used for engineering verification of spacecraft status only. The compression range of 0.25 to 6 bits per pixel plus lossless compression give considerable flexibility in sequencing MI products to fit within memory and downlink constraints. Small ''thumbnail'' versions of the images are automatically created upon acquisition and usually returned to Earth later during the same sol for rapid verification of image acquisition. The larger full-frame images are typically downlinked over the next few sols, often after the Rover has driven from the target location. All MER camera data are packetized onboard the rover for downlink, then reassembled into data products by the MER ground data system after they are received.

[15] Each day, MI data products are tracked and processed by the MI Payload Downlink Lead (PDL). During the primary mission (first 90 sols), an MI PDL was assigned for each rover. At the end of Spirit's primary mission, the MER project transitioned from staffing operations on ''Mars time'' (shift start times tied to the Martian clock) to staffing on ''Earth time'' (shifts restricted to daylight hours in Pasadena, California). After this transition, it was possible for one MI PDL to complete the downlink assessment and processing for both rovers. The PDL function has been performed remotely at the USGS in Flagstaff since May 2004. The overall flow of MI data processing was described by *Herkenhoff et al.* [2003].

[16] The PDL duties include data processing at both JPL and USGS, evaluating the quality of the images, reviewing event log files for anomalies, selecting best-focused images and requesting quick-look mosaics, managing onboard data products, and monitoring the MI camera state of health. The PDL also generates downlink reports, updates MI data summary spreadsheets, and participates in the daily Science Operations Working Group (SOWG) meetings. During the SOWG meetings, the PDL reports on camera health and gives an overview of MI data received since the last meeting. Each rover transmits engineering telemetry daily, and the PDL reviews these data to assess MI status. Specifically, the PDL verifies that the CCD and camera electronics temperatures recorded during the downlink session are within the survival range (−110°C to 55°C) and monitors the state of the MI dust cover. Camera temperatures are also recorded each time the MI takes an image and reported in the image headers.

2.3. Ground Data Processing

[17] Image data are decompressed by the MER Operational Product Generation Subsystem (OPGS) using the Multimission Image Processing Laboratory (MIPL) ''mertelemproc'' software [*Alexander et al.*, 2006]. The decompressed data are written to Experiment Data Record (EDR) image files and stored on the MER Operational Storage Server file system. As part of the decompression step the ancillary data in the image headers are extracted and saved in the image file as an attached Planetary Data System (PDS) label. Additional image products derived from these original OPGS EDR files include ''Science'' EDRs (MI and Pancam) and Reduced Data Records (RDRs), and include a wide variety of products such as radiometrically corrected images, geometrically corrected images, stereo products, and mosaics [*Bell*, 2004; *Herkenhoff*, 2004; *Maki*, 2004a, 2004b].

[18] The MI OPGS EDRs are further processed utilizing USGS Integrated Software for Imagers and Spectrometers (ISIS) version 2.1, and IDL software written at Cornell University (Ithaca, NY) and at the USGS Astrogeology Team (Flagstaff, AZ). The software currently runs under the Linux RedHat 7.3 operating system. MI Science EDRs in PDS format are generated at JPL by running an IDL program written by the Pancam team [*Bell et al.*, 2006] and modified for the MI. If the original data product onboard the rover was converted to 8 bit before being transmitted to Earth, the OPGS EDR is converted back to 12 bit using an inverse lookup table. Pixels with digital data numbers (DN) of zero and saturated (255 8-bit DN or 4095 12-bit DN) pixels are treated specially by ISIS so that they are not included in averages and other statistical measurements. The image file labels are also updated to reflect the standard label conventions for processing images in ISIS.

[19] A series of image processing steps to import raw data, convert PDS to ISIS format, apply the radiometric correction algorithm, and convert the calibrated images to PDS format are incorporated into two PERL scripts. Each of these scripts invokes ISIS programs to perform the processing that generates Level 0 and Level 1 images. Level 0 images are raw files that have been converted to ISIS format, and Level 1 images are those that have been radiometrically corrected. The first PERL script requires coordination with computer system administrators at JPL to allow access and retrieval of images from their site. This script automatically searches and finds new images that have been copied into the OPGS EDR directory at JPL, and copies them to USGS via File Exchange Interface (FEI). Whenever new files are copied from JPL, an automated procedure file is run to process the images through a variety of programs to create Science EDRs and Level 1 products, and output them to desired directories. Occasionally we receive and create Level 1 files of partial data products. These are reprocessed when the full data products are retransmitted and used to replace the older versions.

[20] Science EDRs are ingested into ISIS by reading and converting PDS image objects in the labels to appropriate ISIS label keywords using a standard MER translation table. The conversion program also creates and assigns a unique image number and stores it as a keyword in the ISIS image labels. Radiometric calibration is then applied to the ISIS files at JPL and at USGS to create Level 1 files. If reference pixel data are returned with the image, they are used to subtract line-dependent offset (or bias) from the image. To minimize downlink data volume, reference pixels are often not returned with each image, and a model of the reference pixels (described below) is used to subtract the offset. In rare cases in which a ''shutter'' image was not acquired and subtracted onboard the rover [*Maki et al.*, 2003], the transfer

Figure 2. MI dark current images taken during first cruise instrument checkout on 17 July 2003. Contrast is enhanced to emphasize subtle features. (top) Zero-second exposure image 2M111743171, showing temporary radiation effects. (bottom) One hundred second exposure image 2M111743832.

smear and zero-second component of the dark current are modeled and removed from the image [*Herkenhoff et al.*, 2004a]. In all cases, the active area component of dark current is modeled and removed using temperature data recorded in the image header. The image is then corrected for "flat field" sensitivity variations [*Herkenhoff et al.*, 2004a], converted to I/F (irradiance relative to a white Lambert surface, illuminated normally [*Danielson et al.*, 1981]; also known as "radiance factor" [*Hapke*, 1993]) and stored as a floating-point array. Finally, PDS compliant Level 1 files are generated for archival purposes. Both ISIS and PDS files are accessible to the science team in support of tactical operations.

[21] Because the MI depth of field is only 3 mm, each image (or focal section) of targets with significant relief has portions that are in focus and other areas that are out of focus. Therefore the PDL generates focal section merges of MI image stacks whenever possible. The focal section merge is an attempt to combine the best-focused portions of all the images in a stack into a single, well-focused image. As part of this process anaglyphs are synthesized, allowing three-dimensional relief to be viewed with red/blue glasses. These products are generated using custom IDL software (described in more detail below).

[22] When an MI mosaic is acquired, there is often interest in creating a "quick-look" mosaic to assist in tactical operations. In this case, the MI PDL sends a request to the MIPL team at JPL, including a list of the best-focused EDRs. The MIPL team then creates the quick-look MI mosaic and notifies the science team. More refined MI mosaics, using calibrated images, are generated on a longer (nontactical) timescale, as described in the data processing section below.

3. In-Flight Calibration

[23] The results of MI calibration activities before the MER launches were summarized by *Herkenhoff et al.* [2003]; detailed results are available in the MI calibration report [*Herkenhoff et al.*, 2004a]. The collection and application of MI calibration data after launch (during cruise to Mars and landed operations) are described in this section.

3.1. Dark Current

[24] Because the MI has no shutter and its dust cover is not opaque, it is not possible to acquire useful MI dark current data on the surface of Mars. The MI is sensitive enough that starlight would affect nighttime images, and the dark current is difficult to measure at low temperatures, so we have not attempted to acquire MI dark current data since Spirit landed. However, dark current data were acquired twice during Spirit's cruise to Mars, on 17 July and 11 November 2003. During cruise, Spirit was encased in its aeroshell, and very little light was expected to illuminate the MI. Analysis of the MI data returned by the instrument checkout sequences indicates that no measurable light was incident on the camera (e.g., Figure 2). The temperature of the MI during the first checkout (CCD at -5.4°C) was higher than during the second checkout (CCD at -21.3°C), providing two data points to compare with the model for dark current temperature dependence. Full frame images and reference pixels were returned, losslessly compressed in each case. The cruise dark current observations are consistent with the dark current model developed using preflight calibration data [*Herkenhoff et al.*, 2004a].

[25] As expected, the dark frames show the effects of radiation, from both the Mössbauer spectrometer and cosmic rays (Figure 2). These radiation sources generate spurious electrons in a few localized pixels, with typical peak amplitudes of a few DN and maximum amplitudes of a few hundred DN. Such radiation effects are present in all

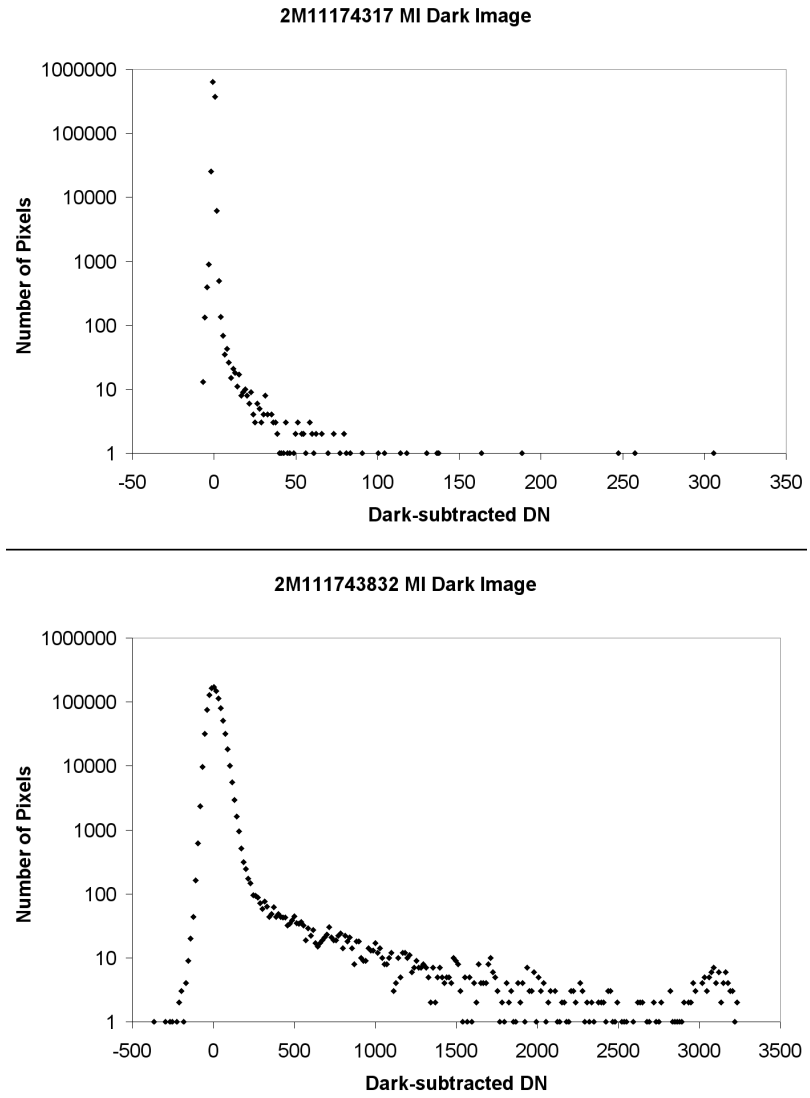

Figure 3. Histograms of MI dark current data acquired during first cruise instrument checkout on 17 July 2003. The MI dark current model was used to subtract average dark current variations from each image. (top) Zero-second exposure image. (bottom) One hundred second exposure image. The increased frequency above 3000 DN is caused by saturation of the pixels.

MI data, but their low amplitude and random spatial distribution makes them very difficult to recognize in images of Mars. To evaluate the statistical effects of radiation on MI images, the MI dark current model [*Herkenhoff et al.*, 2004a] was used to subtract average dark current variations from the instrument checkout images. Histograms of the resulting image data are shown in Figure 3; the asymmetry in the histograms is primarily due to radiation effects. Assuming the shape of the histograms on the left side of the peaks represents the distribution of dark noise alone, radiation affects only 0.04% (~419) of the pixels in the zero-second dark frame (Figure 2, top). In this case, the CCD was affected by radiation only during the 5.2 ms frame transfer time and the 5.2 s readout time. More radiation effects accumulated during the 100-s dark frame (Figure 2, bottom), so that about 20% (~210,000) of the pixels are affected by radiation and some of the pixels are saturated (see right side of Figure 3, bottom). The late cruise dark data show similar levels of radiation effects. These results provide a crude estimate of the effects of radiation on MI data acquired on the surface of Mars: about 2000 pixels are affected per second of exposure time. This rate is expected to decrease during the mission as the Mössbauer reference source decays. Most Spirit MI images were taken with exposure times of less than one second (maximum 1.5 s), so that less than 0.2% of the pixels in a typical MI image will be affected by radiation.

[26] The zero-exposure dark images taken in cruise (Figure 2) also show linear features that are caused by a few slightly "hot" pixels being smeared during image transfer. The hot pixels generate thermal electrons at an unusually high rate. While the capability exists in camera flight software to automatically correct such pixels onboard the rover, the magnitude of the spurious signal generated in these few pixels is too low (less than 5 12-bin DN, or 0.5% of a 1000 DN image) to be a concern. Therefore a

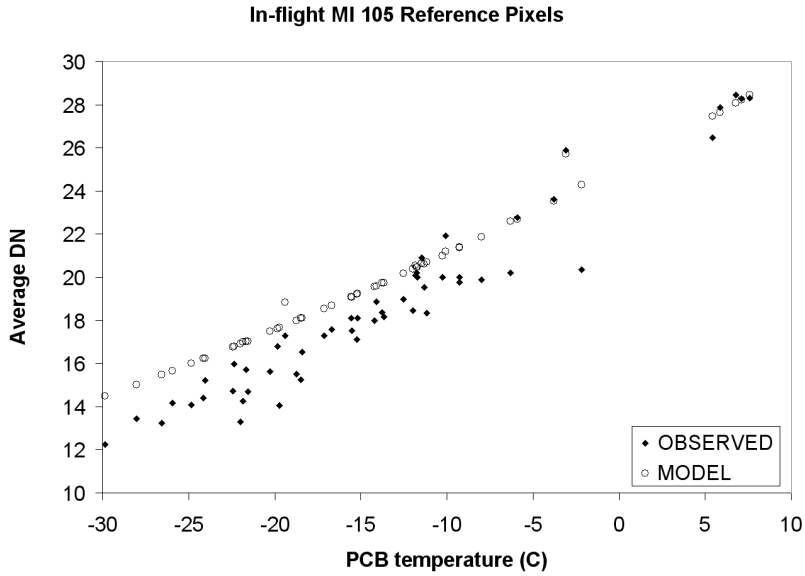

Figure 4. Average of observed reference pixel data in samples 4-14, lines 412-612 compared with model based on preflight calibration data. PCB is printed circuit board in the MI electronics box. The model predictions at −3.1 and −19.4°C that lie above the general trend are for the very long (100 s) exposures taken during cruise.

table of bad pixel locations has not been loaded onto the rover and no correction is made.

[27] The MI CCD temperature was within the calibrated operating range (−55°C to 5°C) for all images acquired during the first 450 sols of Spirit's mission (except for the last 4 MI images acquired on Sol 431, when the CCD was at 12°C). The MI dark current model matches dark (including cruise checkout) data taken below 3°C and with exposure times less than 3 s to within 1 DN. The dark current model was applied to the 100-s MI dark taken during the first cruise checkout, and reduced the standard deviation in a 101 × 101 pixel area at the center of the image from 95 DN to 56 DN. Similarly, the standard deviation in the same area in the 100-s dark taken during the second cruise checkout was reduced from 34 DN to 31 DN. These reductions in noise are not as great as seen when the model was applied to preflight dark images, due partly to a change in the "fixed" pattern of dark noise [*Herkenhoff et al.*, 2004a]; radiation also causes additional noise in the cruise data. Because MI images of the Martian surface were taken with exposure times of 1.5 s or less, the contribution of dark noise to relative calibration uncertainty is less than 1 DN except for the few images that were taken at CCD temperatures above 3°C. Therefore, in the absence of MI dark current data taken after landing, we conclude that dark current subtraction using the MI dark current model is not a significant source of error in calibration of Spirit MI data, typically contributing less than 1 DN to both relative (pixel to pixel) and absolute radiometric calibration uncertainty.

3.2. Reference Pixels

[28] The frame-transfer CCD used in the MI shifts 1024-pixel lines, one at a time, into a serial register during image readout. The MER camera serial register includes 16 additional pixels at each end beyond the 1024 pixels used to receive image data from the CCD [*Bell et al.*, 2003]. These additional pixels are called "reference pixels" and they record the camera offset (or electronic bias, a constant value added to all image data) each time a line of pixels is read out of the MI. The offset of each camera can be adjusted by command, and the Spirit MI (camera serial number 105) video offset was conservatively chosen to ensure that DN values would always exceed zero [*Herkenhoff et al.*, 2004a]. MI reference pixel data products were occasionally returned to Earth to verify that data clipping at 0 DN did not occur and to check the MI offset correction algorithm. The reference pixel data acquired after landing show that zero-clipping did not occur. These data are compared with the reference pixel model developed using preflight calibration data in Figure 4. Reference pixel averages are commonly 2 DN lower than the model and are always within 4 DN, with a standard deviation of 1.7 DN. Hence the magnitude of the error in applying the reference pixel model to MI data for which reference pixels were not returned is small (less than 1% for a well-exposed image).

[29] The variation in reference pixel values with line number changed during flight relative to the typical variation observed in preflight calibration data, with a maximum standard deviation of 0.9 DN at line 1024. Therefore the maximum calibration error for MI images returned without simultaneous reference pixels (including dark current and offset errors described above) is 2.6 DN.

3.3. Sky Flats

[30] As described in the MI calibration report [*Herkenhoff et al.*, 2004a], test schedule constraints did not allow flat field images to be acquired after integration of the MI dust cover. It was therefore necessary to determine the flat field sensitivity of the camera/dust cover combination using in-flight data. Images of the Martian sky, or "sky flats," can be used as flat fields [*Reid et al.*, 1999] if variations in

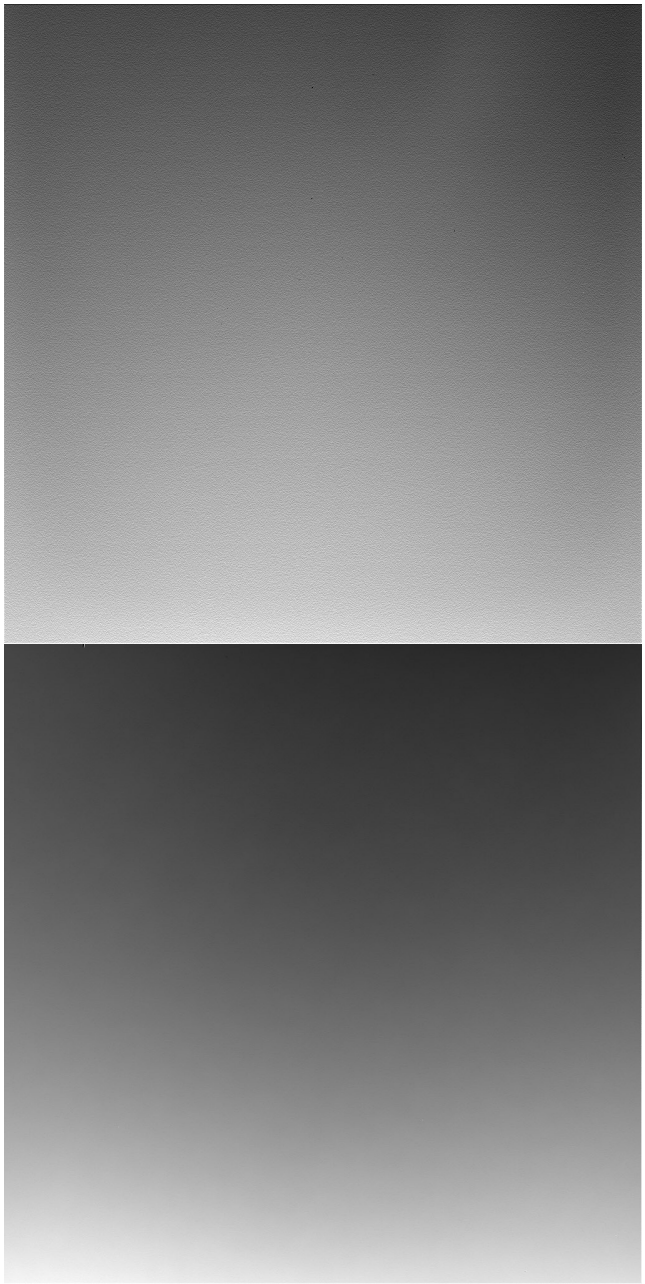

Figure 5. Sky flats acquired on Sol 46. (top) MI image 2M130464431, taken with dust cover open, corrected for dark current. Note subtle structure near upper right corner. (bottom) Left Navcam image 2N130464578, radiometrically calibrated.

sky brightness can be quantified or modeled. To evaluate possible variations in sky brightness over the Spirit landing site, Navcam images were acquired at the same time as MI sky flats, showing the same patch of sky observed by the MI.

[31] The first set of MI/Navcam sky flats were acquired by Spirit on Sol 13, soon after rover egress from the lander. Unfortunately, these images were taken at a solar scattering angle of only 35°, so that scattering of sunlight within the camera optics was significant. Similarly, a single MI sky flat acquired on Sol 419 (with the dust cover closed), taken at a solar scattering angle of 55°, includes ghosts and other evidence of scattered sunlight. MI and Navcam sky flats acquired on Sol 46 at a solar scattering angle of 108° showed no evidence of scattering of sunlight in the optics (Figure 5) and were therefore used to measure the flat field response of the MI with the dust cover open and closed. The MI sky flats were corrected for transfer smear by subtracting a ''shutter'' image onboard the rover, then corrected for dark current using the reference pixel data returned with the images and a model of the active area dark current. The left Navcam sky flat image was similarly processed and radiometrically calibrated by MIPL [*Alexander et al.*, 2006], and the part of the image that viewed the same patch of sky as the MI sky flats was extracted. The Navcam sky flat was then low-pass filtered to remove noise but preserve the variation in sky brightness across the image, and normalized to the average of the central 101 × 101 pixels. The dark-corrected MI sky flats were then divided by the low-pass-filtered, normalized Navcam sky flat to remove variations in sky brightness. The resulting image shows a slight vertical gradient (Figure 6) that was not observed in preflight calibration data and is unlikely to be due to a change in response across the CCD. The gradient may be caused by differences in the variation of sky brightness between the MI and Navcam band passes (570 versus 650 nm) or errors in the Navcam flat field calibration. Further analysis of sky images, including those acquired later in the mission, is required to resolve this issue. Therefore we have not used the Sol 46 MI sky flats to update the flat field calibration files for the dust cover open state. However, these data are useful in deriving the flat field calibration file for the dust cover closed state.

[32] To determine the flat-field response with the dust cover closed, Sol 46 sky flats taken with and without the dust cover were corrected for dark current. The image taken through the dust cover was then divided by the image taken without the dust cover; the result is shown in Figure 7. This closed/open ratio image is used to correct MI images taken through the dust cover as follows: Images taken with the dust cover closed are radiometrically calibrated using the preflight data described above, then corrected for flat field by dividing by the ratio image. Close inspection of the sky images shows the effects of radiation; these effects have not been removed from the ratio image. The standard deviation of the central 101 × 101 pixels in the processed Sol 46 sky flats is 3.4%, greater than the 2.9% standard deviation in the same region of preflight flat fields taken at room temperature [*Herkenhoff et al.*, 2004a]. Thermal noise should be less in the Sol 46 sky flats (acquired when the CCD was at −12°C) than in the preflight flat fields taken under ambient conditions. The increase in noise is therefore probably caused by the radiation effects discussed above. Hence we use preflight flat field data to correct for pixel-to-pixel sensitivity variations in MI images, with the additional correction for images taken with the dust cover closed. When this calibration method is applied to the Sol 46 sky flats, the noise in the central 101 × 101 pixels is reduced to 0.7%. This result indicates that the relative (pixel-to-pixel) radiometric calibration accuracy for this camera is better than 1%, except in localized areas where radiation contributes noise.

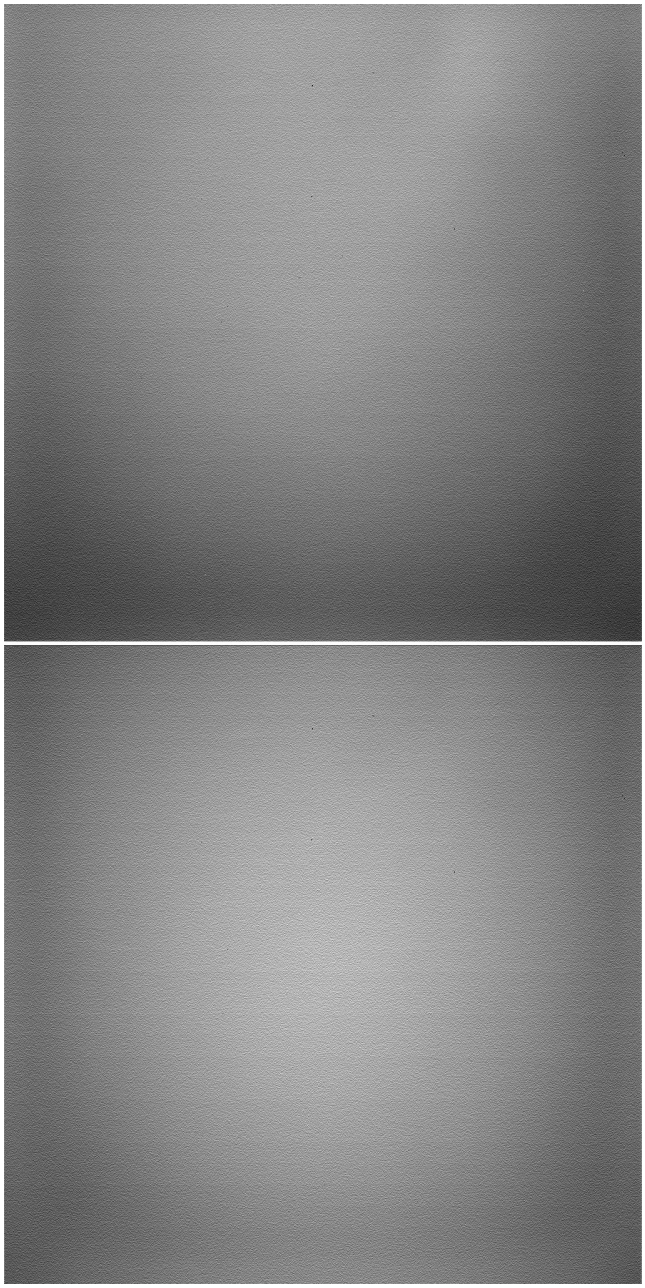

Figure 6. MI flat fields. (top) Processed sky flat acquired on Sol 46. (bottom) Processed flat field acquired during preflight calibration.

3.4. Calibration Accuracy

[33] The absolute radiometric accuracy of the MI is being evaluated by comparing simultaneous images of the Martian sky obtained by Pancam and MI during the second (Earth) year of Spirit operations. The results of this analysis will be reported in a future publication. The relative (pixel-to-pixel) radiometric calibration accuracy is typically of greater interest to users of MI data, as it limits the ability to distinguish and measure small features in the images. On the basis of the results summarized above, the relative radiometric accuracy of well-exposed (>400 raw DN), calibrated MI data is ±1.5%. The error in overall bias/offset correction when reference pixels are not returned with the image data is not included in this value, as it does not affect relative radiometric calibration accuracy.

[34] The MI data obtained during the first 450 sols of Spirit's mission do not show any evidence for changes in geometric calibration at the level of accuracy measured before flight. Therefore the geometric calibration results reported by *Herkenhoff et al.* [2004a] are believed to be valid: The Spirit MI pixel scale is 30.5 ± 0.9 microns and the radial distortion is less than 0.33 ± 0.03 pixel.

4. MI High-Level Data Processing

[35] Although the MI calibration is being updated using in-flight data, we recommend that users of MI data start with Level 1 products, available from the Planetary Data System (PDS), as described below. The archived Level 1 products have been corrected for dark current and offset, flat field variations, and have been calibrated to I/F. These products can be quantitatively compared to other radiometrically calibrated MER camera data and theoretical scattering models.

[36] Higher-level MI products have been generated using various types of software, as described below. We are in the process of validating these products for public release via the PDS.

4.1. Focal Section Merges

[37] Over every target to be observed with the MI we generally take a stack of 3, 5 or 7 images to assure the focus of all segments of the scene in one or another image. These images are taken at different distances from the target and

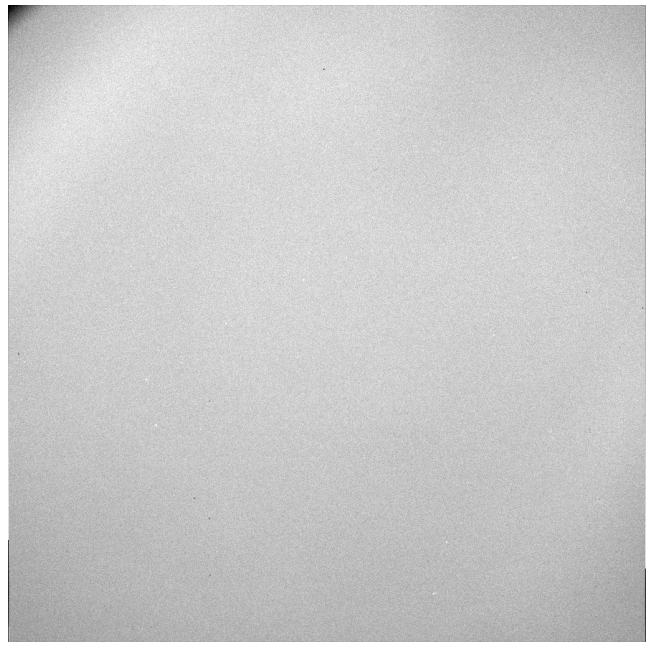

Figure 7. Ratio of dark-corrected sky flat taken with dust cover closed to dark-corrected sky flat taken with dust cover open. Both images acquired on Sol 46. The vignetting at upper left is caused by black tape that was added to the MI dust cover to enable images taken through the cover to be easily recognized.

hence have different scales. In this section we describe two approaches to merging these ''focal sections'' into a single image that shows all parts of the target in good focus. First, the method developed at NASA Ames is described, followed by a description of the method developed by Athena Science Team Member Mark Lemmon.

[38] As a consequence of the IDD having only 5 degrees of freedom there can be a rotation and/or translation of the MI image centers. To understand this set of images and to merge them into a single optimal image it is necessary to first optimally align these images. The NASA Ames software introduces a homographic transformation that aligns each of the images of a given stack. In general, after these transforms the images align very well. However, because the images were taken at different distances there is a difference in parallax as a consequence of the 3D nature of the imaged surface. Effectively, parts of the scene will obscure features in some scenes and not others. In order to effectively build an image that is a merge of images from different focal positions it is necessary to adjust the images for this parallax. This is done in the next stage of the processing of the Ames procedure. Then the set of aligned and parallax-corrected images can be merged into a single image with the best-focused regions used from the images. This step is done by comparing measures of focus sharpness from each segment of each image and then merging the best-focused regions into a single image. In addition there are tools the Athena team uses to browse the aligned and parallax-corrected images and the focal merged image [*Sargent et al.*, 2005].

[39] The other focal section-merging algorithm was designed for use in the tactical operations process and was coded in IDL. The objectives were to provide a quick look at the target in a single frame, to provide synthesized stereo imaging of the target, and to use a subset of the data to determine whether additional images onboard the rover should be downlinked or deleted.

[40] The focal merging concept is straightforward: out-of-focus images of a scene have less high spatial frequency information than in-focus images of the same scene. The actual amount of high frequency information varies across the scene and among scenes; there is no threshold that distinguishes in-focus from out-of-focus. For each neighborhood (any region several pixels across) within a scene, each of the images is considered. The image that has the largest high frequency component is judged to be the best-focus for that neighborhood. The three-dimensional position is then defined on the basis of the pixel coordinates for the neighborhood and the known depth to best focus. The three-dimensional position is refined by a polynomial fit in depth as described below, resulting in depth resolution less than the sampling interval.

[41] The focal merging software relies on a user-compiled list of input images. Several properties render series and individual frames unsuitable: images badly out of focus have no depth information; images with missing packets cannot be included during initial processing, but can be included in archival products after data retransmission; images with shadows often fool the software to varying degrees. In general, any artifact that results in a sharp boundary within a scene that varies from image to image will result in artifacts in the output. In many cases, imaging the MI shadow is unavoidable and the artifacts must be accepted.

[42] The images processed are generally EDRs to allow rapid access. All images are read into memory. The raw digital numbers (DN) are divided by exposure time, resulting in somewhat uniform brightness levels despite possible small changes in exposure time due to auto-exposure. Without any reprojection, the full 1024×1024 image is passed through a simple high-pass filter by dividing the image by a smoothed version of the image (11×11 pixel boxcar average) and subtracting unity. This high-pass image is the basis for determining depth. Dividing the image by the smoothed image eliminates any effect of large-scale illumination variations, but does not eliminate the effect of moving shadow edges. When possible, images are obtained entirely in shadow. For many images, this is not possible, and the moving shadow of the MI itself causes local artifacts in the subsequent processing.

[43] The user selects at least 4 tie points on features that are obvious in multiple images. Each selected tie point is refined using a local feature-matching algorithm so that the relative position of features in the different images is known to at least one-pixel accuracy. The relative positions of the tie points are used to determine the relative altitudes of the MI in the various images (through variation in image scale) and any twist around the optical axis (through image rotation) caused by the fact that the IDD has 5 degrees of freedom, not 6. Generally, the IDD motion includes very little twist. The full 6-degree of freedom position and orientation of the MI is determined from the tie points, to correct small errors in the actual versus planned position of the IDD turret.

[44] All images are then rescaled with bi-cubic convolution interpolation such that tie points are aligned with their location in the best-focused image of the stack. The rescaling is done separately for both the set of raw (DN/s) images and high-pass images.

[45] The processing proceeds in two stages. A first approximation of depth is determined by simply looking up, for each pixel in the aligned images, which image has the largest absolute magnitude of high-frequency component. Pixels are not compared to other pixels, as the true high-frequency component can and does vary across the scene. But for a specific pixel, the image in which the high frequency component is maximized is taken to be the image with that pixel in focus. The depth for each pixel is then set to be the altitude corresponding to the in-focus image (the constant offset for pupil-to-target distance for best focus is ignored, as all depth information is treated as relative within the same scene). At the end of this stage, an in-focus image is created by assembling the best-focus raw image value (DN/s) for all pixels into a new image.

[46] The first stage results in a depth map at the resolution of IDD motion, with typically 3 to 7 different altitudes used for one focal series and 3 mm steps. The amount of high frequency information is generally a smooth function of altitude (i.e., the depth of field is fairly well sampled). The second stage increases the depth resolution by going back to each pixel and performing a second order polynomial fit to find the altitude of best focus. Because each pixel in the high pass filtered version has some information from neighboring pixels and because of inherent noise in the process, a 5×5 pixel median filter is used to eliminate

outliers, and the depth map is smoothed with a 15 × 15 pixel boxcar average. The final horizontal resolution in the depth map is therefore near 15 pixels, or 0.46 mm. Repeat image sequences of the same target suggest depth repeatability is ~1/5 the step size, or ~0.6 mm. Finally, the in-focus image is updated by polynomial interpolation of the raw images in depth to the best-focus position.

[47] The primary output of this procedure is a merged image that is, in principle, all in focus. This image is saved as a TIF file named "⟨id⟩_raw.tif", where ⟨id⟩ is a text identifier chosen by the operator. The first ancillary product is a depth map, saved as "⟨id⟩_dem.tif" and "⟨id⟩_dem.txt". The text file contains scaling factors that convert the 0-255 range within the TIF to elevations in mm (with an arbitrary zero point). The depth map is then used to project the image into synthetic left and right eye views, archived as "⟨id⟩_[RL].jpg". The projection is a simple shift of pixels values left or right depending on depth. The magnitude of the shift is dynamic, such that the full range of depths in the image is displayed. The projection results in variations in vertical exaggeration, so the DEM files should be used rather than the anaglyphs for quantitative assessment of topography. The right and left eye views are combined into an anaglyph for stereo viewing, "⟨id⟩_ana.jpg". Examples of merged MI images and an anaglyph are shown in Figure 21. These products are available on the MER Analyst's Notebook (see section 4.7) under "Additional Data Sets."

4.2. MI Cover Open/Closed Color Composite

[48] Early in Spirit's mission, MI images were often taken with the dustcover in both the open and closed positions. Synthetic color products are created by applying various processing techniques. The closed dustcover image is coregistered to the open dustcover image first. The open dustcover image taken from about the same height as the closed dustcover image is typically used because the relative distortion between the two images is minimized, improving the performance of the coregistration software.

[49] The first method produces a false-color file by assigning the closed dustcover image to the red filter, and the open dustcover to the green filter. The blue filter image is generated by subtracting the closed dustcover image from the open dustcover image.

[50] The second method creates a quasi-natural color file. The different colors are assigned as follows:

$$\text{Red} = 0.0072 \times \text{Open dustcover image} + 0.9285 \times \text{Closed dustcover image}$$

$$\text{Green} = 6.6548 \times \text{Open dustcover image} - 4.7273 \times \text{Closed dustcover image}$$

$$\text{Blue} = 10.6699 \times \text{Open dustcover image} - 8.2406 \times \text{Closed dustcover image}$$

The coefficients above were obtained by using the calibrated spectral sensitivity curves for the MI camera with cover open and closed to calculate the expected response to each of a set of reference spectra. Spectra of typical Mars soil and rock were taken from *Maki et al.* [1999], and a flat (white) spectrum was used as a third reference. The visual response to each of these reference spectra was approximated by the spectral reflectance at a wavelength near the sensitivity peak for each visual receptor, 440, 550, and 700 nm, respectively [*Pratt*, 1978]. This is a convenient approximation made reasonable by the smoothness of the reference spectra. The modeling problem is overdetermined (i.e., it is not possible to calculate intensities in 3 wavelength bands from only 2 inputs), so the coefficients were selected to give the best least-squares approximation of the red-green-blue values for each reference spectrum from the corresponding MI open and closed responses. The overall normalization of the coefficients is arbitrary and was chosen so that the sum of red, green, and blue values equals the sum of open and closed inputs for a flat spectrum.

[51] After each color file is created by one of these methods, they are stacked into a single cube file, and masked to the area of common coverage among all the bands. The ISIS cube files are converted to JPG format after an acceptable product is made. Various products are generated by setting different stretch values for each RGB component. The minimum and maximum DN values are set to the same values for all three bands for the quasi-natural color file. An enhanced color file is created by saturating 0.5% percent of the pixels at both the low and high ends of the histogram, as shown in Figure 24.

4.3. Stereogrammetry

[52] MI images can be acquired from multiple locations to form stereo image pairs. Topographic measurements can then be made on features in the stereo images, and used to generate a digital elevation model (DEM). Camera distortions can be removed to create an orthorectified image, and when combined with a DEM, topographic distortions can also be removed.

[53] The location of the MI is tracked relative to the rover: IDD joint angles allow the position and orientation of the MI to be determined. We use the MI geometric data generated in SPICE format by JPL's Navigation and Ancillary Information Facility. The positioning of one MI image relative to another using SPICE kernels is accurate to within a millimeter. To remove these small errors the images are transferred to a commercial photogrammetric workstation running SOCET Set software (®BAE Systems) where triangulation is used to determine the position and orientation of one image relative to the other images.

[54] Information on the MI position and orientation is passed from the SPICE kernels into SOCET Set. This information is then translated into a format that SOCET Set can understand. We define a rectangular coordinate system relative to one MI camera position and transfer the camera position and orientation angles from the coordinate system(s) used in ISIS to a coordinate system used by SOCET Set. Within ISIS, processing of MER images is done in the local level frame [*Maki et al.*, 2003]. The ISIS environment employs a target definition file to describe the characteristics of the target that was imaged. For orbital images, the target definition file contains the size, shape, and orientation of the planet. For lander images, the target can be soil or rock surfaces. To handle this situation, the

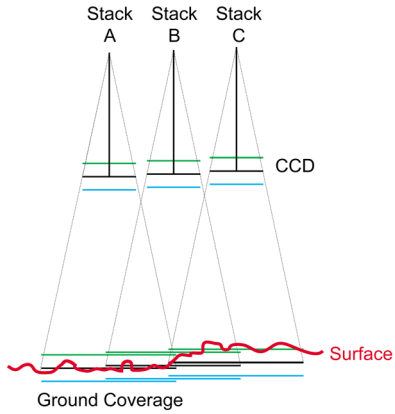

Figure 8. Schematic diagram of overlapping stacks of MI images used to acquire stereo coverage of surface.

target definition file contains a description of a plane. Each lander image can have its own target plane definition, or a set of images can share a target plane definition.

[55] SOCET Set works in a right-handed coordinate system for which the positive Z-axis is "up" and camera angles are entered either in the photogrammetric omega-phi-kappa system, or as heading-roll-pitch. The MER local level frame is a right-handed system, but with the positive Z-axis "down" along the gravity vector. Simply rotating the local level frame so that Z is up is not adequate for SOCET Set, because in the local level frame, camera pointing in the direction of the horizon can result in orientation angles near 90°, which we have found to be problematic in SOCET Set. SOCET Set works best if we establish a coordinate system that simulates imagery acquired by a nadir-pointing camera. For the MI case, this can be achieved by defining a target plane that is approximately normal to the MI boresight for all images in an image set.

[56] Specifically, for a given set of MI images, we start by defining an "in-focus-plane" as our target plane in ISIS. The in-focus-plane is calculated from a single image (chosen by the analyst) and defined at the best-focus distance from the camera. In the target definition file, the origin and spanning vectors of the plane are described in local level frame coordinates, but the orientation of the plane is normal to the MI boresight (for the chosen image). This target plane defines the orientation of our coordinate system, which still has the positive Z-axis down. We then rotate the coordinate system so that the positive Z-axis is up. Furthermore, to yield a user-friendly definition of (x, y, z) coordinates in SOCET Set, we translate the coordinate system (in the target definition file) so that (0, 0, 0) is in our established target plane. Elevations (along z axis) in SOCET Set are then relative to the target plane, with positive z values above the plane (closer to the camera), and negative z values below the plane. The resulting coordinate system corresponds to the Local Space Rectangular (LSR) coordinate system used in SOCET Set.

[57] With the coordinate system defined, the camera positions are rotated and translated from local level frame into the LSR coordinates for SOCET Set. The remaining step is to rotate the camera orientation angles from the local level frame to angles relative to our established coordinate system, in the omega-phi-kappa system. The results are camera position and orientation angles similar to those of a nadir pointing camera with respect to the ground or rock surface.

4.3.1. Stacks and Stereo Overlap

[58] Figure 8 illustrates how stacks of images and stereo images are collected. As described above, a stack of MI images is typically acquired to ensure that the ground surface is imaged in focus. By translating the MI camera laterally, another stack of images can be acquired and the overlap area provides a stereo model that can be measured in 3 dimensions. With another lateral translation of 15 mm a third stack is collected that barely overlaps the first stack and provides stereo overlap with the second stack.

[59] Typical patterns in which MI images were collected are illustrated in Figures 9 and 10. For RATted (abraded) areas, a pattern of 5 image stacks were often collected. One image is centered in the circular hole created by the RAT (image labeled 5 in Figure 9). Four additional images are collected that cover the entire abraded surface. Images 1–4 can be mosaicked together and an orthorectified image and DEM can be derived that covers image 5. Variations of the pattern shown in Figure 10 were also commonly acquired. An image stack would be collected at the location shown by image 1 in Figure 10, and at the predicted best focus distance the MI camera would be translated perpendicular to the boresight to acquire a single stereo image at image

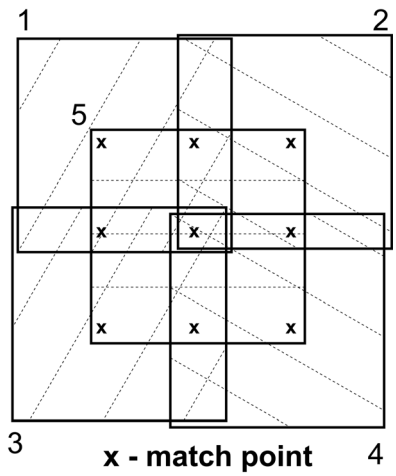

Figure 9. Example of MI image footprints used to cover RAT hole, with partial stereo coverage in center.

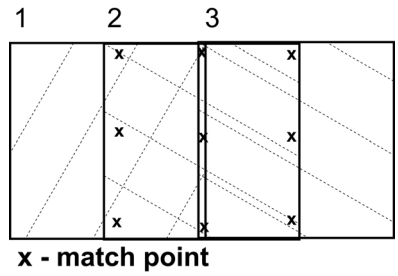

Figure 10. Example of MI image footprints used to acquire partial stereo coverage of 2 × 1 mosaic.

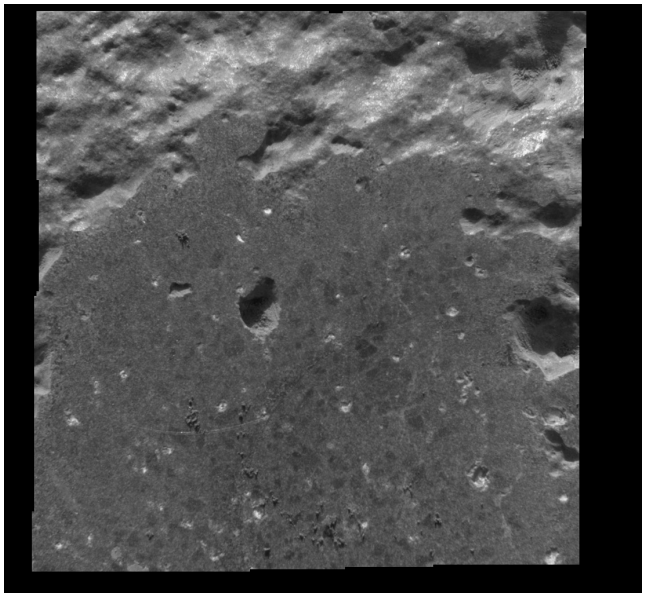

Figure 11. Orthorectified image based on DEM generated from calibrated image 2M131690279 and overlapping images 2M131690648, 2M131690939, 2M131691250, and 2M131691503 acquired on Sol 60. Image resolution is 30 microns per pixel; image is 1017 lines by 1100 samples, or 28 mm high by 29 mm wide. Note dark olivine megacrysts below and right of center, but not at the edge of the abraded surface (near the original rock surface).

location 2. Another stack of images might be acquired at image location shown by the image labeled 3. This pattern was sometimes repeated with stereo images collected at the predicted best focus distance.

4.3.2. Triangulation

[60] There are minor errors in the locations of the MI camera derived from engineering telemetry, which lead to noticeable errors when mosaics are made from the images. To remove the MI camera location errors the images are triangulated. The coordinate system used here is the same as that described in the stereogrammetry section above. The position and orientation of the image that was used to define the in-focus plane ($z = 0$) is held fixed and the other images are adjusted relative to the first image. This is accomplished by selecting match points on identical features in the images (Figures 9 and 10 show typical patterns of match points). The triangulation process solves for the position of the match points relative to the image that was held fixed. The z component of the match point's position can be used to define a plane that can be used when creating a mosaic from the images. For some surfaces, such as the floor of a RAT hole, it might be desirable to define a surface of constant elevation. In these cases, another triangulation can be run. All the images are allowed to change and the z components of some of the match points are held at an arbitrary elevation.

[61] After the triangulation is completed, a DEM can be created from the stereo images. Automatic extraction of the DEM works very well for the general surface and the DEM can to be used for the creation of orthorectified images (Figure 11) or orthomosaics. To capture the fine detail some editing of the DEM is usually required. An example of a DEM generated from MI data is shown in Figure 12.

4.4. MI Mosaics

[62] To generate an MI mosaic, the best-focused images from each stack of an MI mosaic are selected for processing. Archived Level 1 files are converted from PDS to ISIS format. To project the Level 1 images to an orthographic projection, a transformation file that maps out where the pixels are placed in the output file is created. The projection is defined with a standard scale of 0.00003 meter/pixel. The target definition file created previously is used as input. After the transformation file has been created, the program "geom" is run to actually project the Level 1 file to a Level 2 file with a defined map projection and scale. The next step is to create an uncontrolled (no tie points picked) mosaic of all the Level 2 images. First, the x range and y range are determined from the keywords in the image labels. The program "mermos" then creates a mosaic. The output file must be initialized with appropriate x-range and y-range values when the first image is placed into the mosaic. Additional processing can be performed to create a tone-matched product.

[63] SOCET Set provides another tool for the creation of mosaics. The main inputs are images to mosaic, an elevation plane or DEM to project the images onto, the image order (the order in the input list, the lowest image, or a seam database), histogram adjustment, and seam smoothing. Using a DEM will create the best possible mosaic with no noticeable distortions. When projecting onto an elevation plane, selecting the average elevation of the area being mosaic will minimize distortions. The image order is generally set to start with the image closest to the target. This will select the central parts of the set of images first. The seam database option allows the user to select where the seams between images will fall. This can help minimize the visibility of seams by selecting areas where the topography is flat and the texture is smooth. The histogram adjustment option balances the histograms of the images so they appear uniform. An MI mosaic of the target "New York" on the rock "Mazatzal," taken after RAT brushing, is shown in Figure 13. Another MI mosaic of the same target, taken after RAT grinding, was included as Figure 3B of *Arvidson et al.* [2004].

4.5. MI/Pancam Color Merge

[64] A single MI image or an MI mosaic can be merged with Pancam color images. The two products must be coregistered first, and then added together to produce colorized images in which the intensity comes from the MI and color (hue/saturation) comes from the Pancam images. This method of colorizing data may not yield a satisfactory product if the solar illumination is from a different direction in the Pancam relative to the MI images, or if the images are partly shadowed. It can be difficult to find where the MI overlaps the Pancam due to the scale difference (roughly a factor of 20) and differences in illumination, especially for soil targets.

[65] If a single MI image is to be merged with Pancam color, the best-focused MI image in a stack is selected. If an MI mosaic is to be merged, the MI image whose camera orientation was used to create the target definition file and to

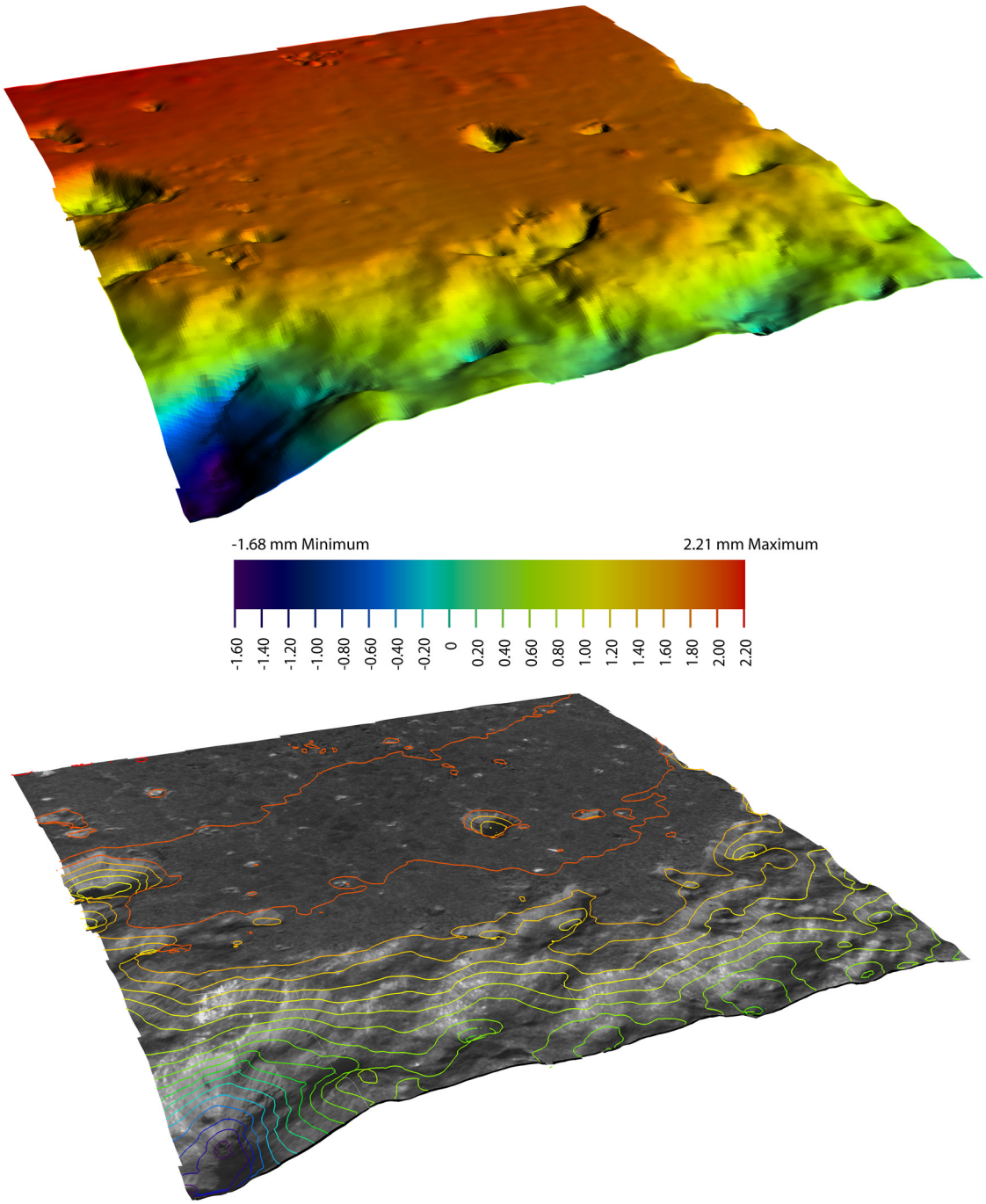

Figure 12. Perspective views of DEM generated from stereo images of abraded surface of target "Heyworth" on rock "Humphrey," acquired on Sol 60. No vertical exaggeration. This DEM was used to create the orthorectified image in Figure 11. Elevations range from −1.68 (purple) to 2.21 (red) mm relative to in-focus plane for image 2M131690279. (top) Color-coded topography with DEM shaded relief image. (bottom) Orthorectified image draped over DEM, with contour lines at 0.2 mm intervals.

project all the MI images to the same plane is used. The Pancam color images that overlap the MI scene are selected, and radiometrically calibrated (I/F) versions are copied from JPL. We typically use Pancam images taken through filters L2 (753 nm), L5 (535 nm), and L7 (432 nm) or L4 (601 nm), L5 (535 nm), and L6 (482 nm) [*Bell et al.*, 2003].

[66] Level 2 files (orthographic projection) of the MI and Pancam data that have the same map scale, x-range, and y-range are then created. The default map scale used to create the orthographic projection is 0.00003 meter/pixel for all the images. This process calculates minimum and maximum x-range and y-range values to create a border around the MI image without cutting off valid data.

[67] If an MI mosaic created in SOCET Set is to be merged with Pancam color data, the orthorectified MI images and orthomosaics are saved as TIFF images with

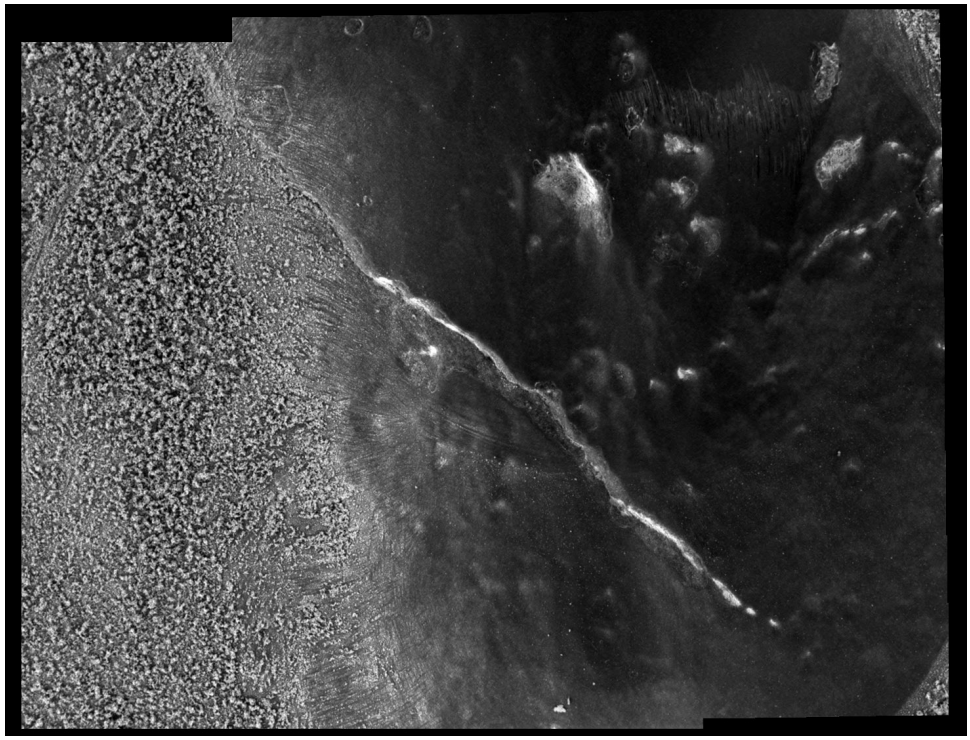

Figure 13. Mosaic of radiometrically calibrated MI images 2M133386183 and 2M133386588, acquired on Sol 79 when the target was fully shadowed. Area shown is 3 cm high.

no label information. The TIFF files are converted to ISIS and the image label information is recovered as follows: First, a sufficient number of pixels must be added around the MI Level 2 image that was used as the in-focus plane. This is done so the SOCET mosaic can be projected into the Level 2 space of the single MI frame. Next, the MI Level 2 image is copied to a new file, and all the valid pixels are set to null. The single Level 2 image and the MI mosaic are then displayed to find where the MI mosaic overlaps the Level 2 image and to make sure the scale is the same for both images. The offset between the two images is calculated and used to mosaic the MI mosaic into the nulled Level 2 file. If the registration is poor, the process is repeated.

[68] To merge MI mosaics with a Pancam image, label information for the mosaic is created by using the plane defined by the MI image that was used to define the in-focus plane. A blank level 2 ISIS image is created with an orthographic projection and that is larger than the MI mosaic image. The MI mosaic is registered to the level 2 ISIS image, and mosaicked onto the orthographic image space, which creates an MI image with label information. The area of valid data is extracted. The Pancam image is projected into the same orthographic projection, the Pancam orthographic images are coregistered to the new MI level 2 image, and if any misregistration remains, then match points are picked to warp the Pancam image to the MI level 2 image. After all the images are coregistered, the MI and the Pancam images are merged creating a new set of red, green, and blue filter images. The tones for the MI images are matched to the Pancam data so the color information of the Pancam is retained. Then final stretches are selected, and a JPEG format file is created.

[69] One of the Pancam images is then registered to the MI mosaic following the same process as above. If the registration is good, then the area that includes the MI mosaic is simply extracted. If the registration is poor, then the Pancam must be warped to the MI mosaic. This step requires the analyst to interactively measure control points that identify the line and sample location of a number of features on both images. The input (from Pancam) and output (from MI) line and sample values are entered into a text file that is then read by the warping program. The MI Level2 and the warped Pancam image are displayed to evaluate the registration. If the features do not align well, more control points are added in the areas with the most offset, and the warping program is run again. When an acceptable registration is achieved, the other two Pancam images are warped using the same input file.

[70] When the registered MI and Pancam images are generated, a script is run that creates the merged MI and Pancam color files. The output file names follow the MER naming convention for processed data products [*Alexander et al.*, 2003]. The keywords are extracted from the labels, and formed into a filename by concatenating the keywords into a string. A text file containing information about the input files is also created following the same naming convention, but with a ".txt" rather than ".cub" extension. The final step is to generate JPEG and TIFF formatted files that resemble the natural color of Mars. When an acceptable product has been created, the stretch pair information is added to the accompanying text file for the MI/Pancam color merge. A quasi-natural stretch of a merge of Pancam color data with an MI mosaic is shown in Figure 14. Other MI/Pancam merges were displayed in the foldout of the Spirit issue of *Science* (6 August 2004).

4.6. Photoclinometry

[71] The two-dimensional photoclinometry (or shape-from-shading) algorithm of *Kirk* [1987; see also *Kirk et al.*, 2003b] allows estimation of surface relief from a single MI image at the limit of resolution. The primary limitations are that variations in surface reflectance will be interpreted as slopes and will lead to artifacts in the topographic model if they are present, and that both the angular distribution of the incident illumination and the photometric behavior of the surface must be well characterized in order to give an accurate relation between image contrast and the amplitude of recovered topography. The second condition is not met with MI imagery (the diffuse illumination field in the shadow of the rover has not been modeled), so the example shown in Figure 15 must be considered to represent relative topography with vertical scaling uncertain. A mean direction of the incident illumination with emission angle 45° and azimuth opposite the rover was assumed, as was a Lambertian scattering law. Neither of these assumptions is likely to be accurate, but they affect mainly the scale of recovered topography. If a stereo DTM of the same area were available, it could be used to calibrate the scale of topography from photoclinometry, as described by *Kirk et al.* [2003a], but this was not possible for the present example. Artifacts in the DTM related to albedo variations were found to be relatively minor, but the ridge running diagonally from top center to lower right was subsequently shown to be an artifact resulting from a reflection off the spacecraft, when a later image showing the same area without the reflection was obtained.

4.7. Archived MI Data

[72] All publicly released Spirit MI data are being archived through NASA's Planetary Data System (PDS; see http://pds.jpl.nasa.gov/). The PDS is an active archive and the nation's major provider of scientific planetary data. MI data archived with the PDS at the time of publication include data for Sols 1-450 [*Herkenhoff*, 2004]. Both science EDRs and RDRs have been produced for individual MI observations. These comprise the data sets to be used by the planetary science community interested in quantitative analyses. Additional releases of RDRs generated from MI data, including mosaics and color composites, are planned to support detailed scientific analyses.

[73] Once data are delivered to the PDS, they are made available to the public via three different PDS data dissemination Web sites:

[74] The Planetary Image Atlas is intended to be used by scientists and other users who are novice users of MER data and who are primarily interested in MI and other image data. The Atlas can be found at http://pdsimg.jpl.nasa.gov/cgi-bin/MER/search?INSTRUMENT_HOST_NAME=MARS_EXPLORATION_ROVER.

[75] The MER Analyst's Notebook is intended for scientists with a good working knowledge of the MER mission who need the detailed information associated with particular science observations: http://anserver1.eprsl.wustl.edu/.

[76] The PDS Data Set Search Page provides a top-level, cross-instrument search of all data resources associated with the MER mission, including the data available via the Planetary Image Atlas and Analyst's Notebook. It also includes direct links to all online archives: http://starbrite.jpl.nasa.gov/pds/index.jsp.

[77] At the end of the MER missions, all MI data delivered to the PDS will be permanently archived on hard media and a copy will be provided to the National Space Science Data Center (NSSDC). This is done to fulfill the PDS, NASA, and MER commitments to ensuring that the data are long-lived and available far beyond the existence of the mission and instrument teams.

5. Overview of Results

[78] The scientific results of MI observations acquired by Spirit through Sol 450 are summarized in this section. Results of the MI investigation during the first 90 sols of the Spirit mission were summarized by *Herkenhoff et al.* [2004b]. More recent Spirit MI observations are also discussed by *McSween et al.* [2006], L. Richter et al. (Surficial crusting of soil-like materials at the MER landing sites, manuscript in preparation, 2006; hereinafter referred to as Richter et al., manuscript in preparation, 2006), *Squyres et al.* [2006], and *Wang et al.* [2006a, 2006b]. Observations of rocks in Gusev crater are discussed below, followed by a discussion of soil observations. In addition, the MI observed Spirit's filter and capture magnets on Sols 92, 150, 151, 240, 258, and 307 (M. B. Madsen et al., Overview of the Magnetic Properties Investigation on Spirit and Opportunity, manuscript in preparation, 2006). The MI was also used to image Spirit's solar panels to assess contamination by dust and sand (see Table A1).

5.1. Rock Observations

[79] Many rock targets in Gusev crater were observed by the MI (see Table A1). *Cabrol et al.* [2006] analyzed MI images to estimate porosity variability in the rocks. These observations suggest that rocks in the Columbia Hills have greater void space than plains rocks. Textural information derived from MI observations of rocks on the Columbia Hills has been used along with other measurements to identify different lithologic types and classify rocks in the Hills [*Squyres et al.*, 2006]. This classification scheme is used in the following discussion of selected MI observations of rocks.

5.1.1. Adirondack Class Rocks

[80] Spirit imaged and analyzed several rocks on the floor of Gusev crater during its first 155 sols on Mars. The rocks are porphyritic olivine basalts that are uniform in bulk composition [*McSween et al.*, 2004, 2006]. Olivine is the only mineral to have been positively identified from analysis by all the IDD instruments. The Gusev basalts are similar to certain Martian meteorites called olivine-phyric shergottites; both contain olivine megacrysts (Figure 11). But unlike the shergottites, the Gusev basalts display abundant vesicles, indicative of eruptive flows with some volatile component. Some of these vesicles are partly filled by lighter-toned, presumably secondary minerals (Figure 11). Figure 11 shows a lack of olivine megacrysts near the original surface of the rock "Humphrey" after RAT grinding, indicating that weathering and breakdown of olivine has obscured the primary rock mineralogy [*McSween et al.*, 2006]. Therefore olivine-rich basalts produced from eruptions of primary magmas may constitute a

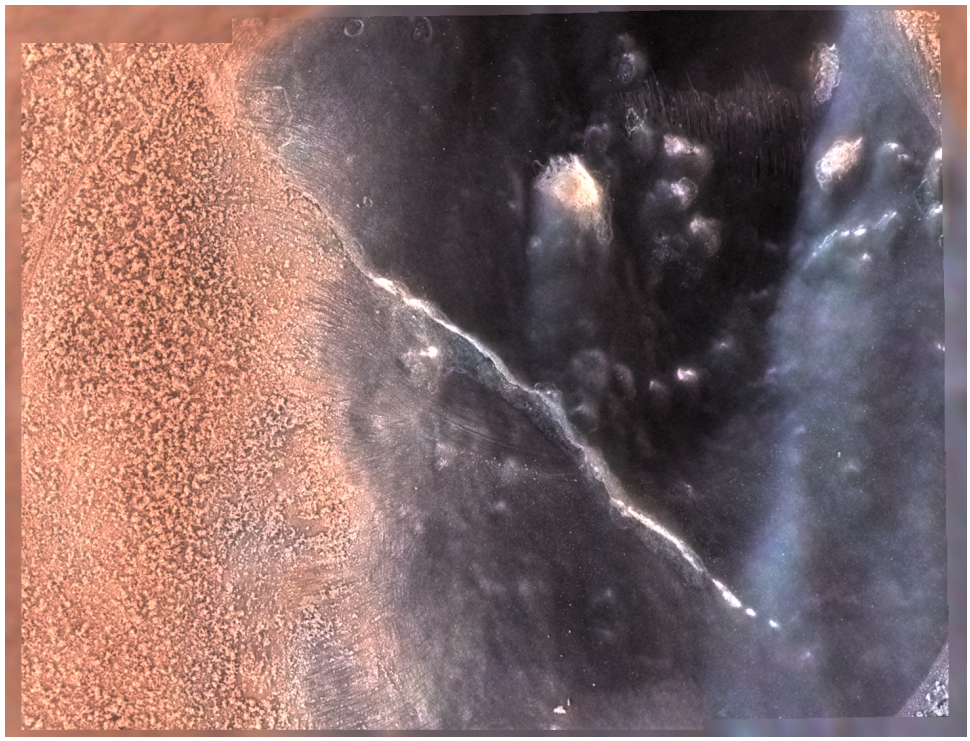

Figure 14. Merge of MI mosaic shown in Figure 13 with radiometrically calibrated Pancam color images 2P133549862 (filter L4, red channel), 2P133549894 (filter L5, green channel), and 2P133549906 (filter L6, blue channel). Area shown is 3 cm high.

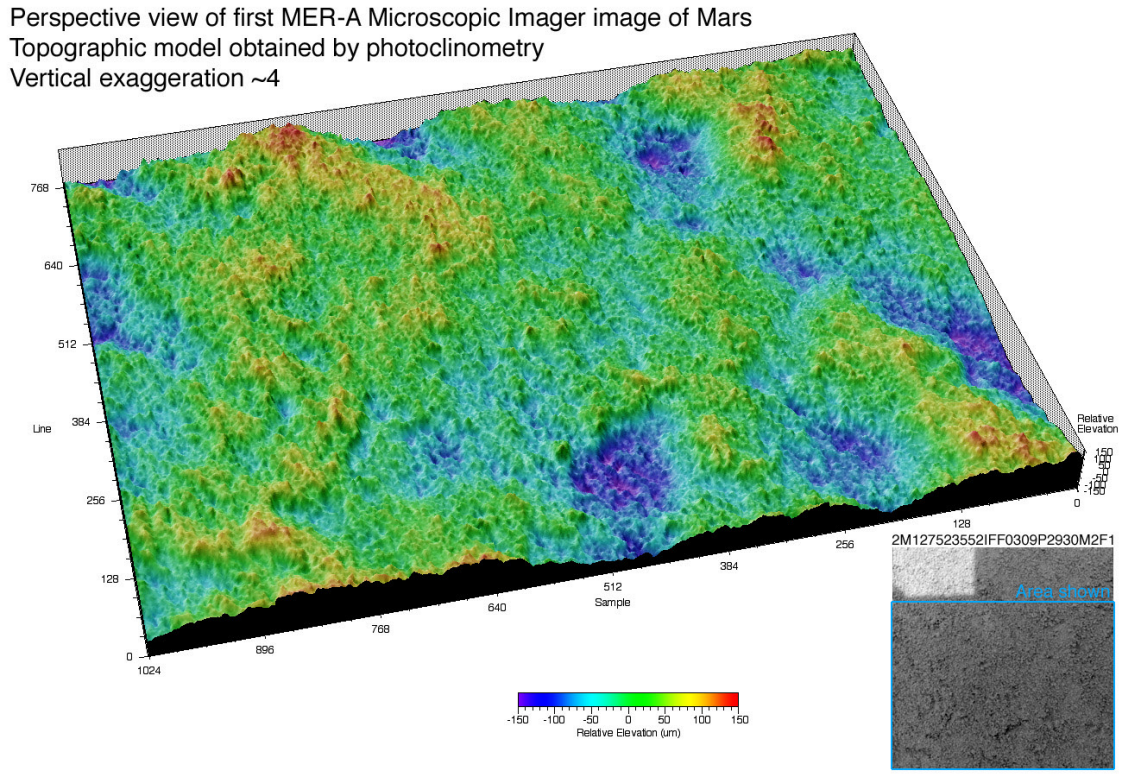

Figure 15. MI photoclinometric DEM generated using lower part of image shown at lower right (3 cm across).

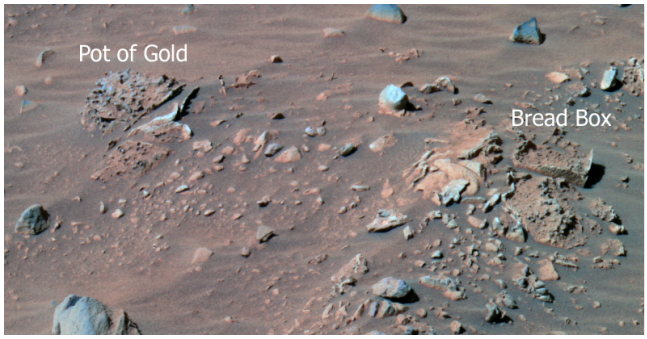

Figure 16. Pancam color composite of radiometrically calibrated subframed images of rocks in "Hank's Hollow" acquired on Sol 158. Note resistant rind, evidence for case hardening, below "Bread Box" label at right.

significant portion of the Martian crust, yet remain difficult to detect in orbital remote sensing data due to alteration [*McSween et al.*, 2006].

[81] The nearest volcanic source for the Gusev basalts appears to be Apollinaris Patera [*Martínez-Alonso et al.*, 2005], a moderate sized volcanic cone about 250 km north of Gusev crater and assigned a Hesperian age. Although distance and topographic gradient pose significant questions regarding Apollinaris Patera as a source for these basalts, no other volcanic vents closer to Gusev have been identified. *Nyquist et al.* [2001] and *Borg et al.* [2001] have radiometrically dated olivine-phyric shergottites ranging from 175 to 575 Ma, ages that place them in the Late Amazonian Period. Thus it appears that the Gusev basalts are significantly older (Hesperian or early Amazonian in age) than the olivine-phyric shergottites (Late Amazonian). Along with differences in composition these two factors would suggest there is no direct petrogenetic relationship between the Gusev picritic basalts and olivine-phyric shergottites [*McSween et al.*, 2006].

5.1.2. Hank's Hollow

[82] Spirit's arrival at Hank's Hollow signaled an important transition from the volcanic geology of the younger intercrater plains to the older rocks of the Columbia Hills [*Arvidson et al.*, 2006]. This transition was marked by the appearance of unusual rock surface weathering features not previously seen along Spirit's traverse. Of special interest were the rocks Pot of Gold, Bread Box and a number of smaller unnamed rocks, all of which exhibited case hardened exteriors, with cavernously weathered (core softened) interiors (Figure 16).

[83] Case hardening of terrestrial rocks involves interactions between two processes [*Dorn*, 2004]: (1) the softening of the rock interior by selective leaching of soluble components and (2) selective cementation of a rock exterior at fracture surfaces. The addition of cements locally increases the induration of a rock, enhancing resistance to weathering and erosion. Subsequent physical and chemical weathering tends to differentially etch the surface of the rock, bringing the more resistant, better-cemented areas into relief. On Earth, case hardening is most commonly seen in sandstones that have undergone arid weathering [*Campbell*, 1999]. However, case hardening has been observed for a broad spectrum of other rock types (granites, basalts and metamorphic rocks) over a broad range of climatic conditions (wet tropical, arid and alpine glacial [*Dorn*, 2004; *Goudie and Viles*, 1997]). Thus climate and lithology are less important to these processes than the specific rock-water interactions that lead to selective cementation of a rock. In terrestrial settings, the common factor in case hardening is the late diagenetic migration of fluids along joints or other

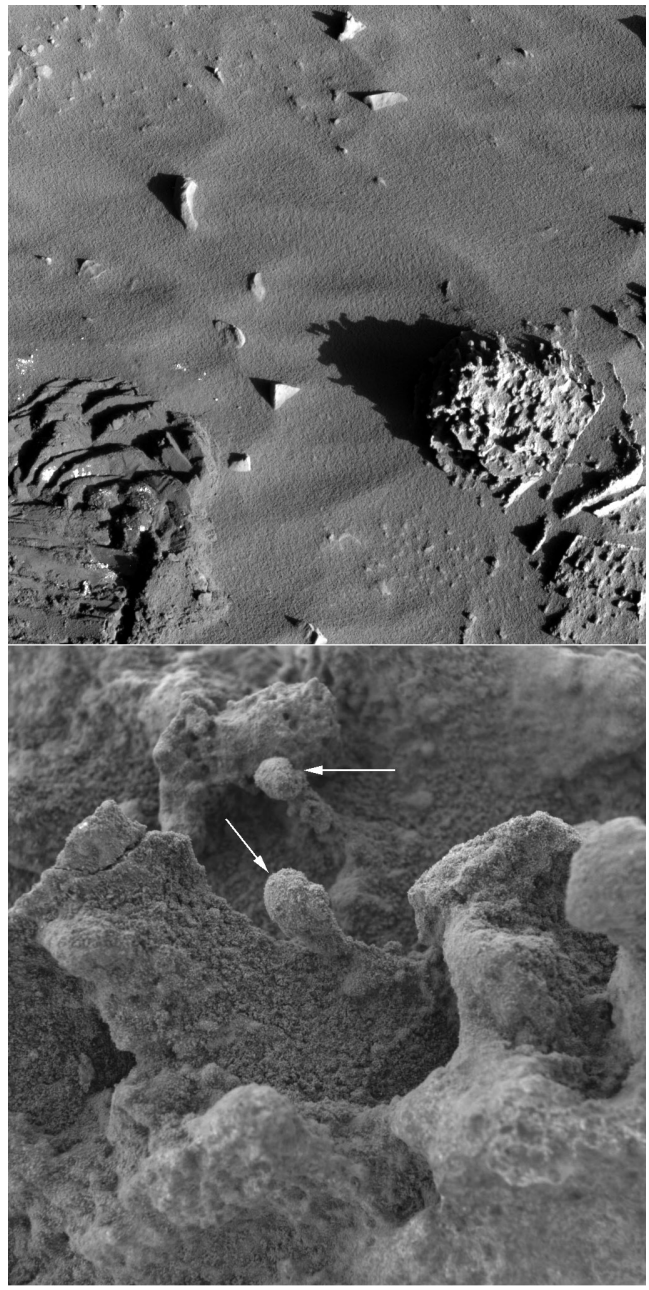

Figure 17. Radiometrically calibrated images of "Pot of Gold" in "Hank's Hollow." (top) Left Pancam image 2P140936727, taken through blue filter (L7) on Sol 164. Rock "Pot of Gold" at right is about 14 cm across; rover wheel tracks shown at lower left. Illumination from lower right. (bottom) MI image 2M141460980 of part of "Pot of Gold," taken on Sol 170 when target was is full shadow. Field of view is 3 cm across. Note nodules (arrowed) supported by septa.

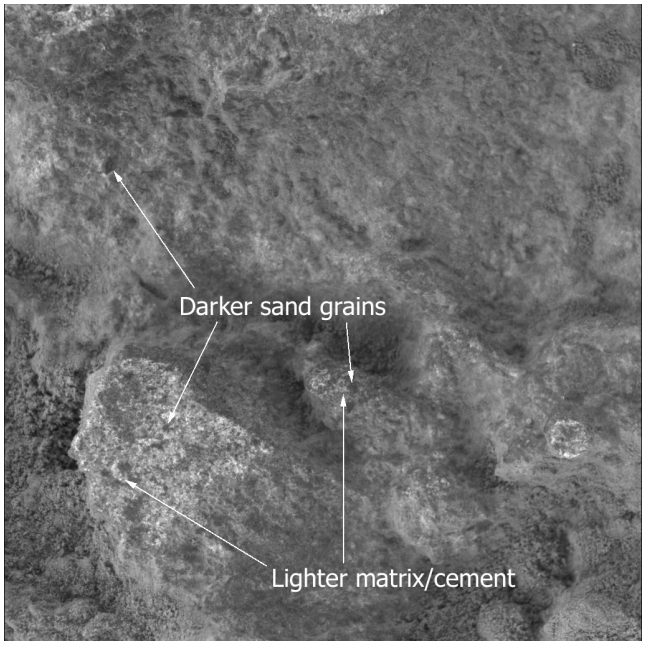

Figure 18. Radiometrically calibrated MI image 2M141460980, acquired on Sol 171 when the target "Pot of Gold" was fully shadowed. Field of view is 3 cm across.

fractures, accompanied by the deposition of cements and fracture filling precipitates to form case hardened exteriors. The most common terrestrial cements involved in case hardening are silica plus aluminum, iron and/or manganese oxides.

[84] Case hardening of rock exteriors is often accompanied by a development of core softened rock interiors and often, a type of cavernous weathering known as tafone (pl. *tafoni*). This unusual form of cavernous weathering is especially common in coastal areas where salt spray penetrates into porous rock surfaces. In tafone weathering, the rock surface develops a distinctive honeycombed texture, with irregular rounded cavities, separated by narrow septa. Although still debated, the origin of tafoni appears to require capillary-driven, salt-mediated weathering processes where normal granular disintegration is accelerated by the expansive forces of salts crystallizing within pore spaces [*Charola*, 2000].

[85] Pot of Gold and Bread Box may provide examples of case hardening of rocks on Mars. In these examples, the process appears to have occurred along preexisting joints in the parent rock that were later in-filled with chemical precipitates that cemented the rock matrix adjacent to fracture walls. The textures shown in Figure 16 suggest that rocks adjacent to Bread Box and Pot of Gold may have shared common fractures, the blocks splitting and rotating into their present positions after being exposed at the surface. The most heavily cemented regions of these rocks appear to have since been etched into relief by the wind, with the interiors having been largely removed by wind erosion (see below).

[86] Beneath the case hardened exteriors of Pot of Gold and Bread Box are interior core-softened regions dominated by cavernous weathering. However, it is noteworthy that the cavernous weathering seen in these rocks is not typical tafone weathering. Rather than the usual honeycombed texture, with rounded chambers separated by narrow septal walls, the interior of Pot of Gold consists of an irregular thicket of mm-sized, stalked protuberances generally inclined in the same (perhaps upwind) direction (Figure 17, top). Located at the end of each stalk is a subspherical "nodule" that is more resistant to wind erosion than the surrounding matrix (Figure 17, bottom). Nodules combine to form a resistant cap that appears to protect their connecting stalks from erosion, thereby promoting development of a spinose texture. The exact origin of these nodules is unclear. They could be tiny concretions (more heavily cemented micro-domains within the rock). However, given the observed weathering styles, it seems more likely that they represent areas not as heavily leached, i.e., places in the rock that retain more primary cement.

[87] The original lithology of Pot of Gold is also open to interpretation. MI images obtained of the partly RATted surface on Sol 171 (Figure 18) suggest the rock has a clastic texture. (Although more subtle, this same granular texture is also visible on most weathered surfaces). This interpretation is supported by the occurrence of dark-colored, subrounded grains of fine sand, surrounded by a very fine-grained, light-toned matrix (interpreted to be cement). APXS elemental abundances suggest that Pot of Gold is basically basaltic in composition, but enriched in sulfur [*Gellert et al.*, 2006]. In addition, Mössbauer spectra indicate the presence of hematite [*Morris et al.*, 2006]. These data are consistent with the presence of sulfate and iron oxide cements.

[88] An alternative to the sedimentary hypothesis posits that the parent lithotype was a basaltic volcanic rock that has been subjected to pervasive chemical alteration. This alteration left behind only tiny (sand-sized) resistant remnants of the original rock, which now float in a matrix of lighter toned alteration products. However, given what we know of the processes of case hardening and cavernous weathering on Earth, which require the migration of fluids through a porous and permeable host rock, it seems more likely that the original rock was detrital and not a dense, essentially impervious lava.

[89] On the basis of the above considerations, the parent rock for Pot of Gold is inferred to have been volcaniclastic sediment of basaltic composition that experienced an early phase of acid sulfate weathering. This early aqueous weathering event introduced pervasive, light-toned sulfate cement, which lithified the rock. This cementation process would have necessarily preceded the development of open fracture systems (perhaps formed by impact or crustal unloading). Whatever their origin, these fractures provided conduits for the movement of subsurface water. As fluids moved through the fractured rocks, early-formed sulfate cements were selectively leached from the surrounding rock matrix, while mafic mineral grains were altered to hematite. As fluids moved through open fractures, they deposited minerals, preferentially cementing the rock matrix adjacent to the fracture walls. This selective cementation produced case hardening of fracture surfaces. With surface exposure and weathering, mass wasting separated adjacent joint blocks along preexisting fracture planes, exposing their interior surfaces to aeolian abrasion. Saltating sand grains acted on these variably cemented (differentially leached) interior surfaces to produce cavernous weathering.

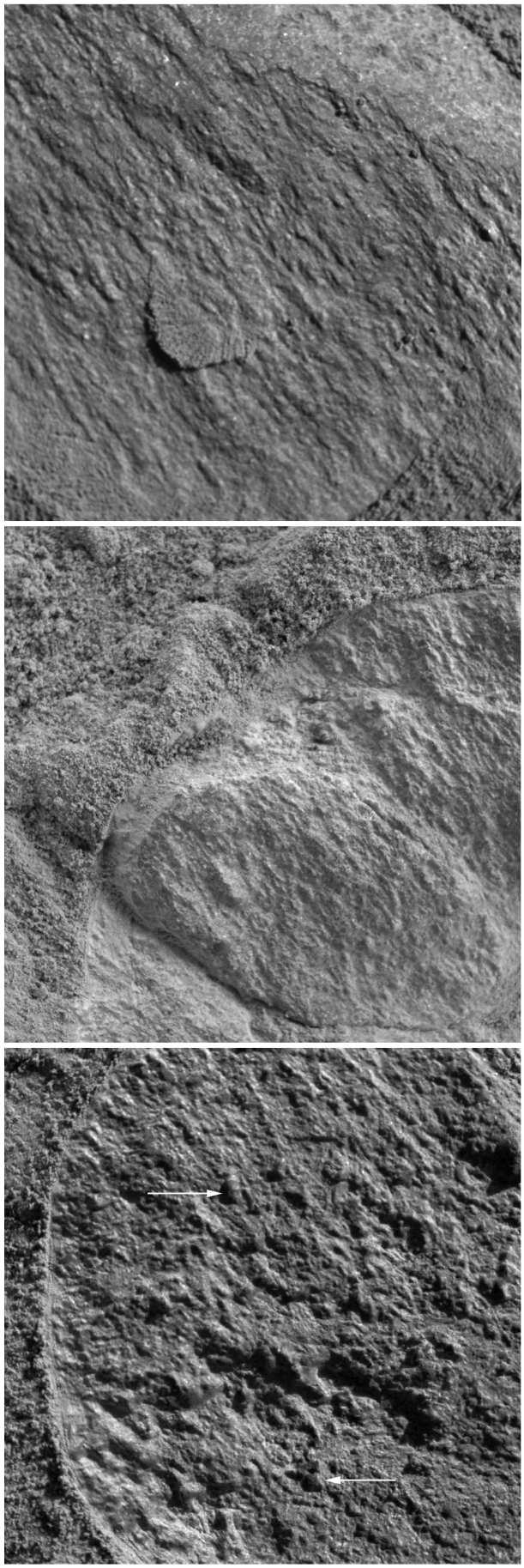

[90] Although the parent lithotype and postdepositional processes that affected Pot of Gold, Bread Box and related rocks at Hank's Hollow are debatable, certainly the case hardening and cavernous weathering produced by these processes argues strongly for alteration by subsurface water. These rock-water interactions selectively removed early-formed cements from the interior rock matrix, concentrating them along fracture walls. The fact that water played such an active role in the postdepositional history of these rocks of the Columbia Hills greatly enhances the potential for subsurface habitability of microbial life during the earlier history of Gusev crater.

5.1.3. Clovis Class Rocks

[91] Three separate targets on the outcrop "Wooly Patch" were observed by the MI, two of which (Sabre and Mastodon) were imaged both before and after RAT abrasion. The natural surfaces of all three targets were covered by dust agglomerates, as commonly observed in Gusev crater. Grains resolved in abraded surfaces are poorly sorted, and appear to be set in a matrix of grains that are too fine to be resolved by the MI. No foliation or bedding is visible. MI and other observations of "Wooly Patch" are discussed in more detail by *Wang et al.* [2006b]. Elemental abundances in the rocks at Hank's Hollow and Wooly Patch suggest that they are mixtures of plains basalts and alteration products [*Arvidson et al.*, 2006].

[92] As Spirit climbed Husband Hill, a variety of rock textures were visible to the MI. Several rocks were subjected to in situ examination on the West Spur of Husband Hill. Surfaces that had been brushed by the RAT sometimes showed textures indicative of foliation or fine-scale bedding (Figure 19). MI images of abraded surfaces of rocks show poorly sorted clastic textures, with grain shapes ranging from angular to rounded (Figure 20). These observations are consistent with the interpretation that these rocks originated as volcaniclastic or impact-generated debris that has been altered and lithified [*Squyres et al.*, 2006].

[93] In contrast to these massive rocks, images of Tetl showed fine layers of ~0.5 cm thickness which have differentially eroded leaving a ridged surface [*Arvidson et al.*, 2006, Figure 14b]. Constituent grains are mostly unresolved by the MI and thus <0.1 mm in diameter. Tetl may have formed from an episodic airfall ash deposition, and differential erosion of the layers may indicate variation in welding of ash fall or result from later chemical alteration along layer boundaries. Alterna-

Figure 19. MI images of rocks in Columbia Hills, taken after RAT brushing. Each image is 3 cm across. (top) Radiometrically calibrated image 2M146348689 of rock "Clovis," taken on Sol 225 with illumination from upper right. Image slightly out of focus, but foliation or bedding is visible trending from upper left to lower right. (middle) Merge of 5 images of target "Chiikbes" on rock "Uchben," taken on Sol 291 when target was fully shadowed. Foliation/bedding less pronounced, but in same orientation as top image. (bottom) Merge of 5 images of target "Flatfish" on rock "Lutefisk," taken on Sol 299 with illumination from upper right. Grains are poorly sorted, with larger, subangular clasts indicated by arrows.

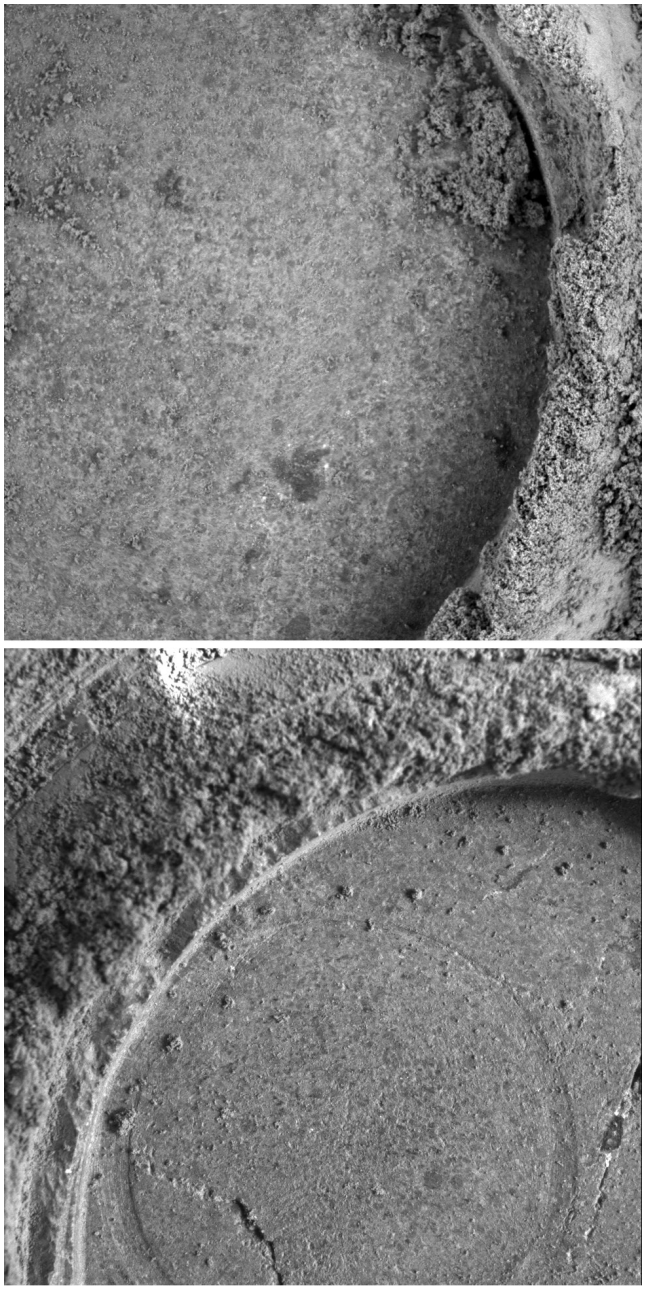

Figure 20. MI images of rock surfaces, taken when target in shadow after RAT grinding. Area shown in each image is 3 cm square. (top) Merge of 5 images of target "Ratchit2" on rock "Ebenezer," taken on Sol 232. Note poorly sorted texture, with angular to subrounded clasts. (bottom) Radiometrically calibrated image 2M151759702 of target "Koolik2" on rock "Uchben," taken on Sol 283. Clasts are generally more rounded than in "Ebenezer."

tively, this rock may record multiple episodes of deposition of impact ejecta.

5.1.4. Wishstone Class Rocks

[94] As she continued to explore Husband Hill, Spirit encountered the rocks "Wishstone" and "Champagne" [*Arvidson et al.*, 2006]. These rocks have more vugs or pits than the rocks lower in the Columbia Hills. The RAT was used to abrade the surface of these rocks, and then the MI observed the resulting fresh surface. As shown in Figures 21 and 22, these are poorly sorted clastic rocks consisting of rounded to angular grains. Like the Clovis-class rocks found on the West Spur of Husband Hill, the larger (up to mm-sized) grains appear to be set in a matrix of grains that are too fine to be resolved by the MI. But Wishstone and Champagne contain a wider variety of light and dark grains than the rocks lower in the Columbia Hills. Grains >0.5 mm in diameter are larger and more numerous than those seen lower in the Hills, as seen on abraded surfaces and as

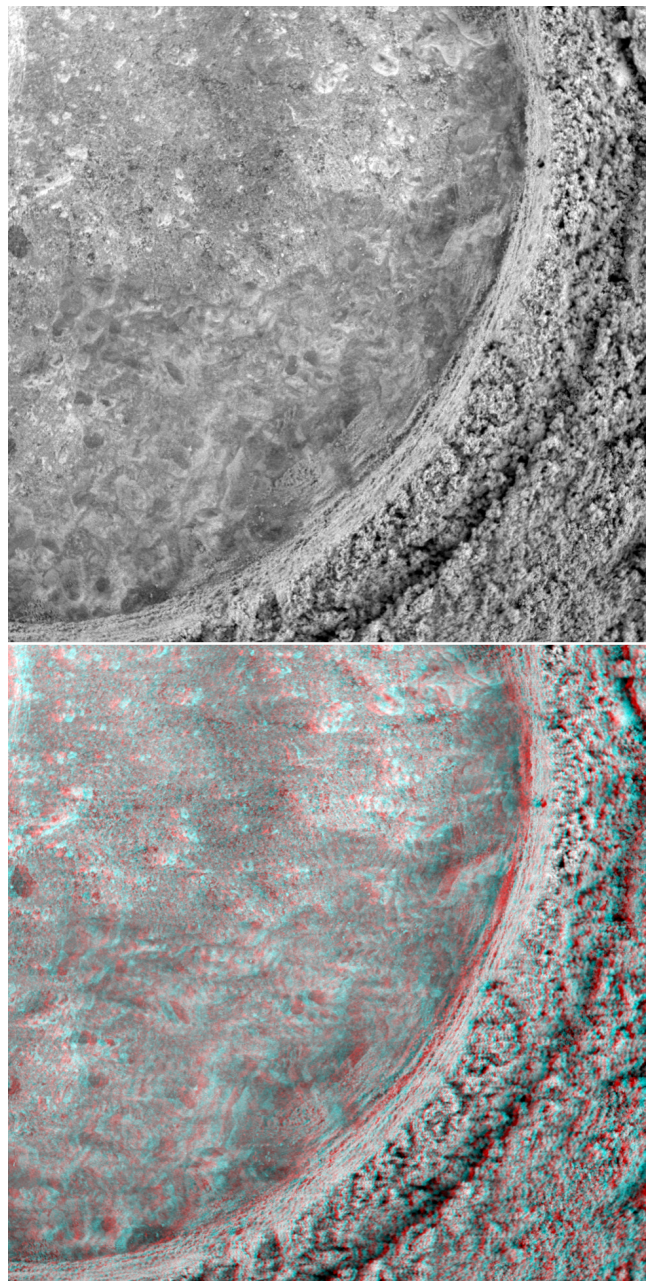

Figure 21. MI focal section merge (top) and red/blue anaglyph (bottom) of part of RAT hole in target "Chisel" on rock "Wishstone." Target was fully shadowed when images were acquired on Sol 334. Area shown is 3 cm across. Note poorly sorted texture, with angular to subrounded grains up to 2 mm in size in a fine-grained matrix.

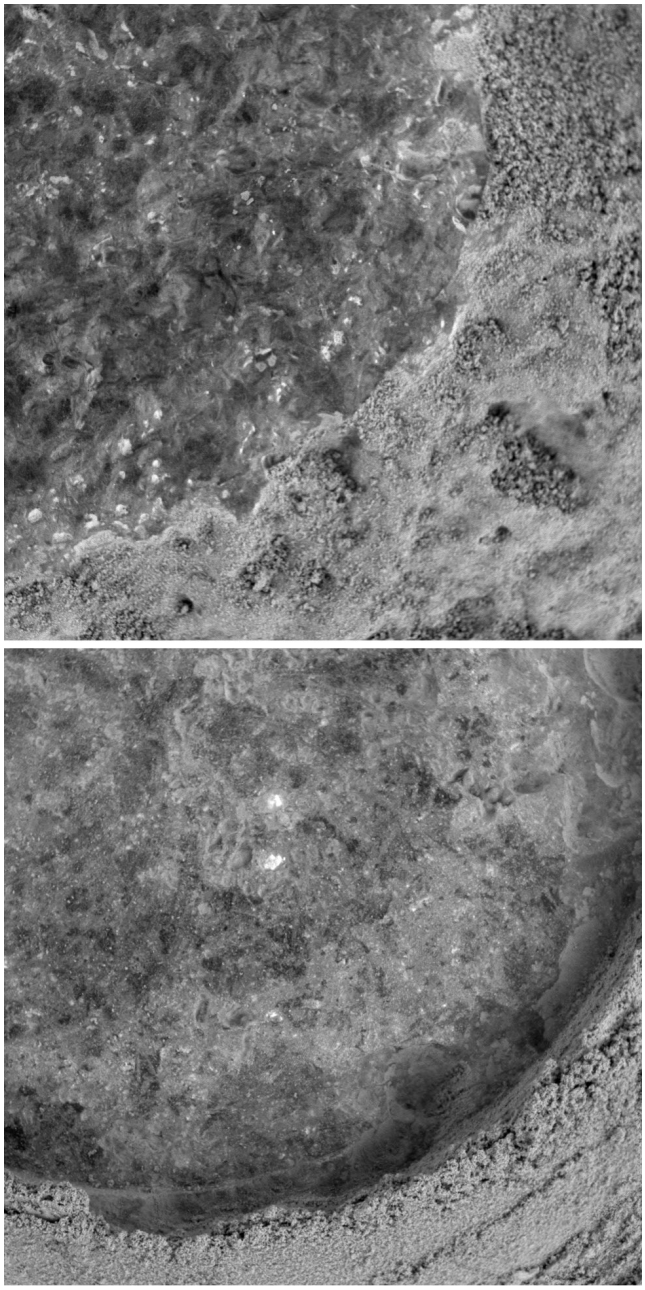

Figure 22. MI images of rock "Champagne," taken in full shadow. Area shown in each image is 3 cm square. (top) Merge of 5 images of target "Bubbles," taken on Sol 354 after RAT brushing. Pits or vugs at lower right are partly filled by dust deposited by RAT brushing of area at upper left. (bottom) Merge of 5 images taken after RAT grinding. Interior of rock is composed of poorly sorted angular to subangular grains, suggestive of high-energy emplacement.

inferred from the comparatively rougher brushed surface where presumably some of these grains have been removed by wind erosion (Figures 21 and 22). Again, these rocks are interpreted to be volcaniclastic rocks, but formation as impact ejecta cannot be ruled out [*Squyres et al.*, 2006].

[95] While substantial textural diversity is evident in MI images, all West Spur rocks and Wishstone-class rocks display characteristics consistent with a volcaniclastic origin. Together with chemical data, these observations are consistent with formation of these rocks by episodic volcanism, with the nature of the material erupted varying over time. Apparent lack of reworking in MI textures indicates either that these materials were wet when they were deposited or were altered following their deposition and lithification.

5.1.5. Peace Class Rocks

[96] MI observations of "Peace" and "Alligator" show that they are finely layered clastic rocks, composed of grains less than a few mm in size. Most of the grains are fine to medium sand size, and the rocks are porous in places. MI images of "Peace" are discussed in more detail by *Squyres et al.* [2006]. These observations are consistent with an interpretation of Peace-class rocks as basaltic sandstones that were cemented by sulfates.

5.1.6. Watchtower Class Rocks

[97] The MI was used to image the target "Joker" on the rock "Watchtower" after RAT brushing (Sol 415) and after RAT grinding (Sol 417). The postbrush images show submillimeter-thick veins that are typically brighter than the matrix surrounding them (Figure 23). Dark, subangular grains are also evident in Figure 23. The postgrind images are dominated by fine grains but show little structure [see *Squyres et al.*, 2006, Figure 10b]. MI images of other Watchtower-class rocks show a variety of textures, as

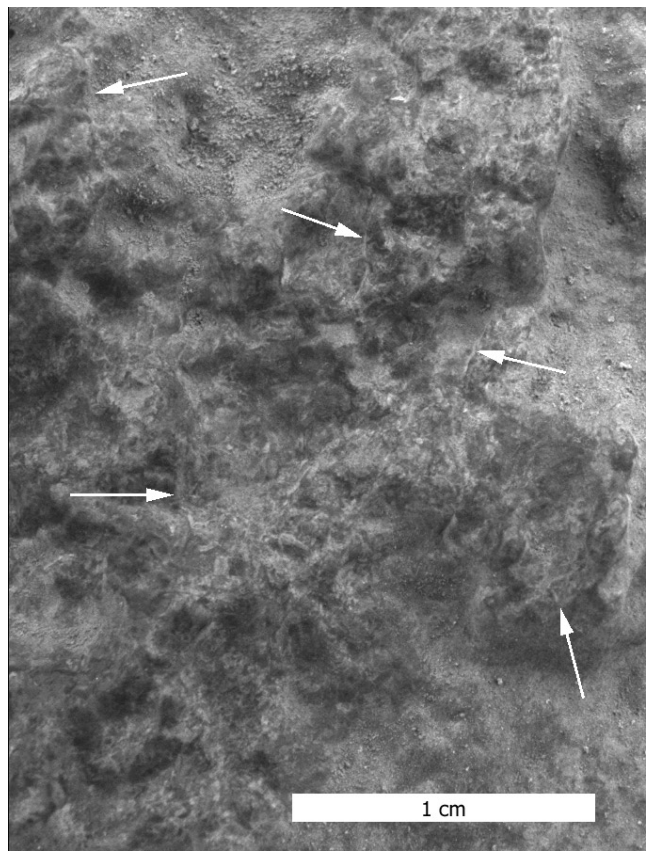

Figure 23. Part of radiometrically calibrated MI image 2M163211218 of target "Joker" on rock "Watchtower," taken after RAT brushing on Sol 415. Small veins marked by arrows. Area shown was shadowed when image acquired.

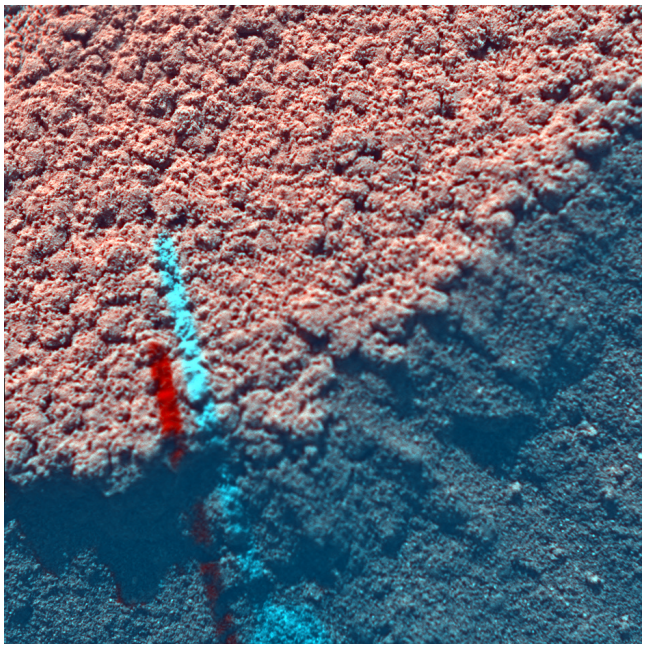

Figure 24. Enhanced color composite of calibrated MI images 2M132842127 (dust cover open) and 2M132842543 (dust cover closed) of target "Kodiak" taken on Sol 73. Natural surface at upper left; wall of trench dug by rover wheel at lower right. Red and blue artifacts left of center caused by shadow of MI contact sensor motion between images. Illumination from top; area shown is 3 cm square. Very coarse sand grains are concentrated at the surface and appear to be covered by bright red clumps of dust.

discussed by *Squyres et al.* [2006]; these observations are consistent with these rocks having formed by impact processes with varying degrees of aqueous alteration. Mössbauer data [*Morris et al.*, 2006] and Pancam multispectral observations [*Farrand et al.*, 2006] also indicate that Watchtower is highly oxidized.

5.2. Soil Observations

[98] The MI has been used to image various soil targets in Gusev crater (see Table A1) to help constrain modes of origin, of weathering, and transport mechanisms of Martian fines. Moreover, microscopic imaging of soils in many instances supports assessments of their physical properties, in particular degree of induration and deformation behavior under load. The term Martian soil is used here to denote any loose, unconsolidated materials that can be distinguished from rocks, bedrock or strongly cohesive sediments. No implication of the presence or absence of organic materials or living matter is intended. *Yen et al.* [2005] discussed four components of the soils observed by Spirit's MI: a thin surficial layer of bright dust, dark soil containing grains 0.1 mm in size and smaller, millimeter-size grains at the surface of bedforms, and larger lithic fragments. They concluded that the bright surficial dust is a globally distributed unit. *Cabrol et al.* [2006] estimated soil grain size distributions from MI images and documented variations along the Spirit traverse. By assuming the fraction of particles not categorized as sand-, granule-, or pebble-sized soils were "fines" (particles below the resolution limit of the MI), they suggested that the proportion of fines was greatest in the upper West Spur region.

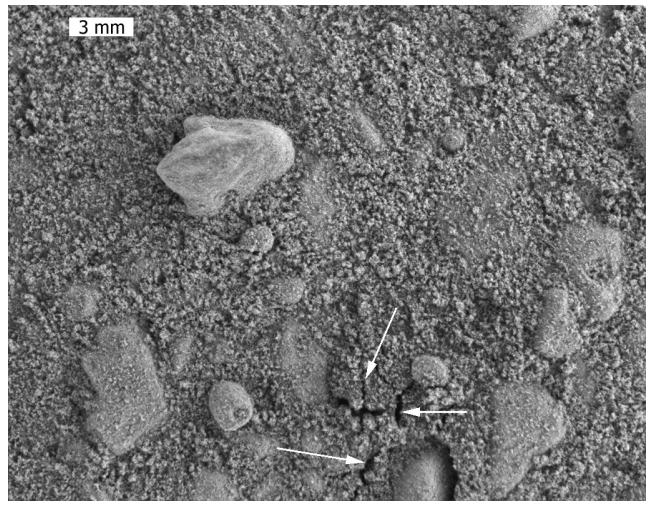

Figure 25. Part of radiometrically calibrated MI image 2M136131725 of target "Soil1" (feature "Waffle Flats") taken on Sol 110 after disturbance by MB faceplate. Granules near bottom of frame have been pressed into fine-grained substrate by the MB and soil shows fracture patterns (arrows) suggestive of a disturbed, indurated surficial layer. Area shown was in shadow when image was acquired; scale bar at upper left.

[99] The bedform "Serpent" was deliberately disturbed with Spirit's left front wheel to expose the interior of this feature [*Arvidson et al.*, 2004]. MI images of "Serpent"

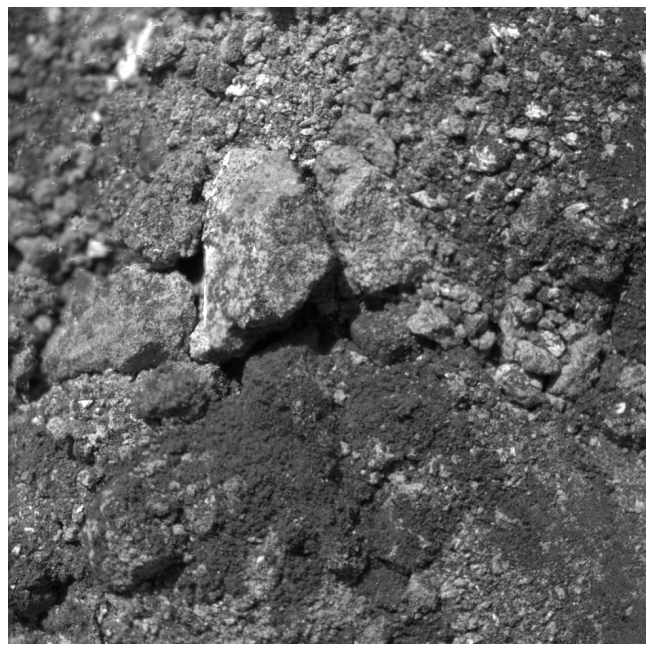

Figure 26. Merge of 5 MI images of target "Shortbread1" (feature "CookieCutter") taken on Sol 181 within a rover wheel track. Illumination from top; area shown is 3 cm square. Area at upper left is out of focus, causing artifacts in merge. Soil appears to contain both bright and dark materials.

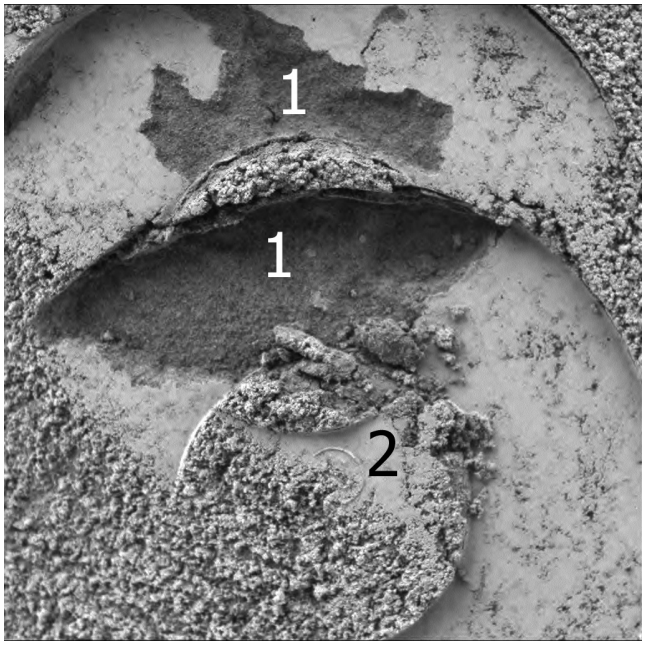

Figure 27. Radiometrically calibrated MI image 2M149359510 of target "Disturbance" (feature "Conjunction Junction") taken on Sol 259 after two-time disturbance by MB faceplate while target was in shadow. Clods of surficial dust layer have been removed by adhering to MB faceplate, exposing relatively darker subsurface soil underneath (1), as previously seen on the plains (e.g., on Sol 54 in image 2M131155133). Imprint of screw head (2) indicates soil is fine-grained and cohesive. Area shown is 3 cm square.

indicate that the surface of this bedform is covered by coarse sand grains that are in turn covered by a sparse layer of dust. Figure 24 shows the edge of the "scuff" or shallow trench. The undisturbed surface appears to be covered by coarse sand with a coating of dust agglomerates. The scuff wall is less red in color because it is not coated by dust, and shows that the interior of the bedform is more poorly sorted than the surface. These observations are consistent with the coarse grains on the surface having been transported in traction, mobilized by the impact of smaller, saltating sand grains [*Greeley et al.*, 2006]. Evidently any aeolian transport ceased some time ago, allowing the dust coating to form by fallout of suspended dust particles. Pancam images of the scuff wall near the left front wheel further suggest that the coarse grains covering the bedform surface are indurated, providing a separate line of evidence for this feature not being active in the current atmospheric regime at Gusev (Richter et al., manuscript in preparation, 2006).

[100] Surface soils on the Gusev plains were periodically surveyed with MI during the long traverse of Spirit from Bonneville crater to the Columbia Hills, spanning the period between about Sols 90 and 156 [*Arvidson et al.*, 2006]. After arrival in the Hills province, soil observations with the MI were less frequent but nonetheless adequate to provide a fair sampling of the surface fines.

[101] Gusev plains soils observed prior to arrival at the Columbia Hills show very little variability and exhibit characteristics very similar to those studied during the primary mission, i.e., essentially covering the traverse from the Columbia Memorial Station to Bonneville crater [*Herkenhoff et al.*, 2004b]. Figure 25 depicts the Sol 110 observation of a typical plains soil after having been disturbed by the Mössbauer spectrometer (MB) faceplate, with some of the granules and clasts having been pressed into the fine-grained substrate constituting the near-surface regolith, which appears to be dominated by silt- and clay-sized particles. The fine-grained fraction shows lines of fracture in the vicinity of the granule pressed into the soil by the MB, supporting earlier observations of thin soil crusts that are easily disrupted when loaded by the rover wheels or IDD instruments [*Arvidson et al.*, 2004].

[102] On the way to the hills, the two trenches "Big Hole" (Sol 113) and "The Boroughs" (Sol 135) were excavated in plains soils with remarkable results from geochemical investigations of the exposed subsurface soils pointing to enrichments of sulfates [*Wang et al.*, 2006a]. MI observations of trench walls and bottoms revealed poorly sorted materials with grains largely below MI resolution and exhibiting slight to moderate cohesion as judged from trench walls and MB faceplate imprints.

[103] Upon arrival at the Columbia Hills West Spur region, the depression dubbed "Hank's Hollow" was the subject of intense interest due to its unusual rocks (discussed above). The soils in the Hollow also showed

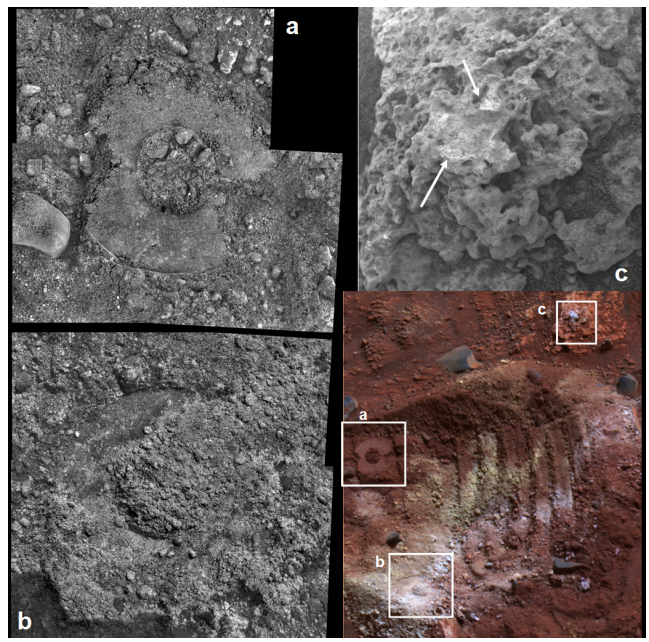

Figure 28. MI images acquired at three locations near the "Paso Robles" soils, with portion of Pancam false-color context image (P2530, Sol 431, L2 (753 nm), L5 (535 nm), and L7 (432nm) filters). (a) Mosaic of four MI frames of "Paso_Dark1" target (Sol 428), showing imprint of MB contact plate; (b) mosaic of four MI frames of "Paso Robles" target (Sol 400), showing less distinct imprint of MB contact plate; (c) radiometrically calibrated MI image of "Ben's Clod," taken after RAT brushing on Sol 429. Arrows indicate fresh surfaces that have been exposed by RAT brushing.

Table A1. Summary of Spirit MI Observations, Sols 1–450[a]

Sol	Starting Image ID	Target	Feature	Target Type	No.	CS	S/M	Relation to RAT/MB	Pancam Sequence
2	2M126553157	NA	NA	Health Check	1	C	M	NA	None
13	2M127522385	Sky Flat	NA	Sky	1	O	M	NA	None
13	2M127522505	Sky Flat	NA	Sky	1	C	M	NA	None
13	2M127523552	FirstSoil1Final	NA	Soil	5	O	M	Pre-MB	p2269, Sol 012
15	2M127691206	FirstSoil1Final	NA	Soil	5	O	M	Post-MB	p2548, Sol 015
17	2M127876303	Prospect	Adirondack	Rock	7	O	M	Pre-Brush	p2382, Sol 030
17	2M127876805	Prospect	Adirondack	Rock	1	C	M	Pre-Brush	p2382, Sol 030
33	2M129296709	Prospect	Adirondack	Rock	7	C	M	Post-Brush	p2563, Sol 033
33	2M129297197	Prospect	Adirondack	Rock	14	O	S	Post-Brush	p2563, Sol 033
35	2M129468450	Prospect	Adirondack	Rock	10	O	S	Post-RAT	p2578, Sol 035
35	2M129469022	Prospect	Adirondack	Rock	1	C	M	Post-RAT	p2578, Sol 035
39	2M129819881	Sideslope2	Squiggle	Drift	1	C	M	NA	p2593, Sol 039
39	2M129820106	Sideslope2	Squiggle	Drift	10	O	S	NA	p2593, Sol 039
41	2M130001180	Crest	Arena	Drift	5	O	M	Post-MB	p2399, Sol 040
41	2M130001510	Crest	Arena	Drift	1	C	M	Post-MB	p2399, Sol 040
41	2M130001727	Trough	Arena	Drift	7	O	M	NA	p2399, Sol 040
41	2M130002290	Trough	Arena	Drift	1	C	M	NA	p2399, Sol 040
42	2M130089167	Lace	Mimi Shoe	Rock	10	O	S	NA	p2538, Sol 042
42	2M130089783	Lace	Mimi Shoe	Rock	1	C	M	NA	p2538, Sol 042
43	2M130169106	Mimi_Tracks2	Mimi Tracks	Soil	10	O	S	Post-MB	p2537, Sol 042
43	2M130169685	Mimi_Tracks2	Mimi Tracks	Soil	1	C	M	Post-MB	p2537, Sol 042
44	2M130267298	Soil1	Ramp Flats	Soil	5	O	M	Post-MB	p2546, Sol 044
45	2M130356065	Halo_01	Angel Flats	Soil	1	C	M	Post-MB	p2408, Sol 044
45	2M130356182	Halo_01	Angel Flats	Soil	5	O	M	Post-MB	p2408, Sol 044
46	2M130463038	Trout 1	Grande Flats	Soil	14	O	S	Post-MB	p2418, Sol 047
46	2M130463916	Trout 1	Grande Flats	Soil	1	C	M	Post-MB	p2418, Sol 047
46	2M130464431	Sky Flat	NA	Sky	1	O	M	NA	None
46	2M130464495	Sky Flat	NA	Sky	1	C	M	NA	None
48	2M130618323	WallMIonly1	RoadCut	Trench	7	O	M	Pre-MB	p2418, Sol 047
48	2M130618766	WallMIonly1	RoadCut	Trench	1	C	M	Pre-MB	p2418, Sol 047
48	2M130618952	Below WallMIonly1	RoadCut	Trench	7	O	M	NA	p2418, Sol 047
48	2M130619416	Below WallMIonly1	RoadCut	Trench	1	C	M	NA	p2418, Sol 047
48	2M130620923	Floor3	RoadCut	Trench	7	O	M	Pre-MB	p2418, Sol 047
48	2M130621417	Floor3	RoadCut	Trench	1	C	M	Pre-MB	p2418, Sol 047
49	2M130707168	Floor3	RoadCut	Trench	1	C	M	Post-MB	p2418, Sol 047
49	2M130707421	Dividing Line	RoadCut	Trench	7	O	M	NA	p2418, Sol 047
49	2M130708373	Dividing Line	RoadCut	Trench	1	C	M	NA	p2418, Sol 047
49	2M130708543	MasonDixon	RoadCut	Trench	7	O	M	NA	p2418, Sol 047
49	2M130709093	Wall3	RoadCut	Trench	7	O	M	NA	p2418, Sol 047
50	2M130795909	WallMIonly1	RoadCut	Trench	3	O	M	Post-MB	p2420, Sol 050
50	2M130796193	MasonDixon	RoadCut	Trench	3	O	M	NA	p2418, Sol 047
51	2M130884803	Soil2	Split Rock Flats	Soil	5	O	M	NA	p2421, Sol 050
51	2M130885122	Soil2	Split Rock Flats	Soil	1	C	M	NA	p2421, Sol 050
52	2M130974067	SugarT_1	Sugar	Drift	1	C	M	NA	p2425, Sol 051
52	2M130974187	SugarT_1	Sugar	Drift	5	O	M	NA	p2425, Sol 051
53	2M131077199	Filter Magnet	Rover	Magnet	3	O	M	NA	p2578, Sol 054
53	2M131077515	Filter Magnet	Rover	Magnet	1	C	M	NA	p2578, Sol 054
53	2M131077842	Capture Magnet	Rover	Magnet	3	O	M	NA	p2578, Sol 054
53	2M131078362	Capture Magnet	Rover	Magnet	1	C	M	NA	p2578, Sol 054
54	2M131150911	Ridge1	Wrinkle	Soil	5	O	M	Pre-MB	p2572, Sol 053
54	2M131151413	Ridge1	Wrinkle	Soil	1	C	M	Pre-MB	p2572, Sol 053
54	2M131155006	Ridge1	Wrinkle	Soil	3	O	M	Post-MB	None
54	2M131155257	Ridge1	Wrinkle	Soil	1	C	M	Post-MB	None
55	2M131242017	Heyworth_RAT	Humphrey	Rock	5	O	M	Pre-RAT	p2583, Sol 055
55	2M131242375	Heyworth_RAT	Humphrey	Rock	1	C	M	Pre-RAT	p2583, Sol 055
57	2M131420525	Heyworth_1	Humphrey	Rock	5	O	M	Post-Brush	p2591, Sol 058
57	2M131420828	Heyworth_1	Humphrey	Rock	1	C	M	Post-Brush	p2591, Sol 058
57	2M131421037	RightEar	Humphrey	Rock	5	O	M	Post-Brush	p2591, Sol 058
57	2M131421417	RightEar	Humphrey	Rock	1	C	M	Post-Brush	p2591, Sol 058
59	2M131597743	Heyworth_1	Humphrey	Rock	5	O	M	Post-RAT	p2597, Sol 060
59	2M131598082	Heyworth_1	Humphrey	Rock	1	C	M	Post-RAT	p2597, Sol 060
60	2M131690161	Heyworth_2	Humphrey	Rock	25	O	S	Post-RAT	p2597, Sol 060
60	2M131691742	Heyworth_2	Humphrey	Rock	5	C	S	Post-RAT	p2597, Sol 060
63	2M131952543	Nail4	Plank	Soil	5	O	M	NA	p2530, Sol 063
63	2M131952890	Nail4	Plank	Soil	1	C	M	NA	p2530, Sol 063
65	2M132132493	Soil1	SugarLoafFlats	Soil	3	O	M	Post-MB	p2534, Sol 065
65	2M132132777	Escarpment1	SugarLoafFlats	Soil	5	O	M	NA	p2534, Sol 065
65	2M132133132	Escarpment1	SugarLoafFlats	Soil	1	C	M	NA	p2534, Sol 065
68	2M132401584	Gobi1	Deserts	Soil	5	O	M	Pre-MB	None
70	2M132590791	Gobi1	Deserts	Soil	10	O	S	Post-MB	None
71	2M132663577	Window	NA	Soil	5	O	M	NA	None
73	2M132840736	Polar	Bear Paw	Scuff	7	O	M	Pre-MB	p2557, Sol 073

Table A1. (continued)

Sol	Starting Image ID	Target	Feature	Target Type	No.	CS	S/M	Relation to RAT/MB	Pancam Sequence
73	2M132841379	Spectacle2	Bear Paw	Scuff	7	O	M	NA	p2557, Sol 073
73	2M132841868	Spectacle2	Bear Paw	Scuff	1	C	M	NA	p2557, Sol 073
73	2M132842058	Kodiak	Bear Paw	Scuff	7	O	M	NA	p2557, Sol 073
73	2M132842543	Kodiak	Bear Paw	Scuff	1	C	M	NA	p2557, Sol 073
73	2M132842726	Panda_new	Bear Paw	Scuff	7	O	M	Pre-MB	p2557, Sol 073
74	2M132934791	Polar	Bear Paw	Scuff	3	O	M	Post-MB	p2352, Sol 074
74	2M132935173	Panda_new	Bear Paw	Scuff	3	O	M	Post-MB	p2352, Sol 074
75	2M133017039	Soil2	Patio	Soil	5	O	M	NA	p2562, Sol 075
76	2M133104521	Appendix	Geoff	Dusty rock	6	O	S	Pre-MB	p2566, Sol 076
76	2M133113166	Appendix	Geoff	Dusty rock	4	O	S	Post-MB	None
77	2M133196972	Soil1	Mazatzal Flats	Soil apron	6	O	S	Pre-MB	p2568, Sol 076
77	2M133205985	Soil1	Mazatzal Flats	Soil apron	4	O	S	Post-MB	None
78	2M133285037	Arizona	Mazatzal	Rock	6	O	S	NA	p2574, Sol 078
78	2M133285545	Illinois	Mazatzal	Rock	6	O	S	NA	p2574, Sol 078
78	2M133286074	New York	Mazatzal	Rock	6	O	S	Pre-Brush	p2574, Sol 078
79	2M133382710	Illinois_tweaked	Mazatzal	Rock	10	O	S	Post-Brush (Light)	p2588, Sol 081
79	2M133383410	Illinois_tweaked	Mazatzal	Rock	1	C	M	Post-Brush (Light)	p2588, Sol 081
79	2M133386122	New York	Mazatzal	Rock	10	O	S	Post-Brush	p2588, Sol 081
79	2M133386832	New York	Mazatzal	Rock	1	C	M	Post-Brush	p2588, Sol 081
80	2M133463169	Texas	Mazatzal	Rock	10	O	S	Pre-Brush	p2574, Sol 078
80	2M133463870	Texas	Mazatzal	Rock	1	C	M	Pre-Brush	p2574, Sol 078
82	2M133648272	New York	Mazatzal	Rock	25	O	S	Post-RAT	p2590, Sol 082
82	2M133649889	New York	Mazatzal	Rock	5	C	S	Post-RAT	p2590, Sol 082
82	2M133650507	Oregon	Mazatzal	Rock	5	O	M	Pre-MB	p2599, Sol 086
82	2M133650903	Oregon	Mazatzal	Rock	1	C	M	Pre-MB	p2599, Sol 086
84	2M133825381	PMA (Pointing Error)	NA	Error	42	C	M	Post-RAT #2	NA
85	2M133914563	Brooklyn	Mazatzal	Rock	25	O	S	Post-RAT #2	p2596, Sol 085
85	2M133916255	Brooklyn	Mazatzal	Rock	5	C	S	Post-RAT #2	p2596, Sol 085
85	2M133916997	Hawaii	Mazatzal	Rock	10	O	S	Pre-MB	p2596, Sol 085
85	2M133917351	Hawaii	Mazatzal	Rock	1	C	M	Pre-MB	p2596, Sol 085
89	2M134263041	Shredder	Snowboard	Rock	5	O	M	NA	p2532, Sol 089
89	2M134263385	Shredder	Snowboard	Rock	1	C	M	NA	p2532, Sol 089
89	2M134263587	Rams	TCHS	Rock	5	O	M	NA	p2532, Sol 089
89	2M134263975	Rams	TCHS	Rock	1	C	M	NA	p2532, Sol 089
92	2M134534074	Filter Magnet	Rover	Magnet	3	O	M	NA	p2113, Sol 092
92	2M134534398	Capture Magnet	Rover	Magnet	3	O	M	NA	p2113, Sol 092
99	2M135152796	SoHo	Route66	Rock	10	O	S	Post-Brush	p2544, Sol 100
99	2M135153170	SoHo	Route66	Rock	2	C	S	Post-Brush	p2544, Sol 100
105	2M135687370	Flats1	Bitterroot flats	Soil	5	O	M	Post-MB	p2547, Sol 105
105	2M135687707	Flats1	Bitterroot flats	Soil	1	C	M	Post-MB	p2547, Sol 105
110	2M136126236	Soil1	Waffle Flats	Soil	6	O	S	Pre-MB	None
110	2M136131617	Soil1	Waffle Flats	Soil	3	O	M	Post-MB	p2557, Sol 110
113	2M136401275	Mayfly	Big Hole	Trench	3	O	M	Post-MB	p2404, Sol 116
114	2M136480330	Stonefly	Big Hole	Trench	5	O	M	NA	p2404, Sol 116
114	2M136480799	Brassie	Big Hole	Trench	5	O	M	NA	p2404, Sol 116
114	2M136501831	RS2	Big Hole	Trench	3	O	M	Post-MB	p2404, Sol 116
116	2M136662466	Stonefly	Big Hole	Trench	3	O	M	NA	p2404, Sol 116
122	2M137197561	Owens	Cutthroat	Soil	4	O	S	NA	p2565, Sol 122
126	2M137552836	Leadfoot	TruckinFlats	Soil	3	O	M	Post-MB	p2573, Sol 126
135	2M138357379	HorseFlats	Hillyer	Soil	5	O	M	Post-MB	None
140	2M138789298	Williamsburg	The Boroughs	Trench	7	O	M	NA	p2446, Sol 142
140	2M138789734	Mills3	The Boroughs	Trench	7	O	M	Pre-MB	None
140	2M138790260	Hells Kitchen	The Boroughs	Trench	7	O	M	Pre-MB	None
141	2M138878267	Mills3	The Boroughs	Trench	5	O	M	Post-MB	p2446, Sol 142
141	2M138878638	Fordham	The Boroughs	Trench	7	O	S	NA	p2446, Sol 142
141	2M138879066	Kew Gardens	The Boroughs	Trench	7	O	S	NA	p2446, Sol 142
141	2M138892235	Hells Kitchen	The Boroughs	Trench	3	O	M	Post-MB	p2446, Sol 142
150	2M139687377	IDD Fault	NA	IDD Fault	9	C	M	NA	p2585, Sol 150
151	2M139771015	Joshua	Mojave NP	Rock	3	O	M	Post-MB	p2586, Sol 151
151	2M139771441	Filter Magnet	Rover	Magnet	3	O	M	NA	p2586, Sol 151
151	2M139771750	Capture Magnet	Rover	Magnet	3	O	M	NA	p2586, Sol 151
158	2M140400950	Dark4	Shredded	Soil	1	O	M	Post-MB	None
158	2M140401311	WhiteStripe	RedStripe	Rock	5	O	M	NA	p2595, Sol 158
160	2M140565777	DantesPeak	EndOfTheRainbow	Rock	8	O	S	NA	p2597, Sol 159
160	2M140566333	IDD Fault	NA	IDD Fault	8	O	S	NA	p2597, Sol 159
161	2M140653320	DantesPeak2	EndOfTheRainbow	Rock	6	O	S	NA	p2597, Sol 159
162	2M140752100	GoldKlumpen3	EndOfTheRainbow	Rock	7	O	M	NA	p2597, Sol 159
162	2M140752534	GoldKlumpen5	EndOfTheRainbow	Rock	7	O	M	NA	p2597, Sol 159
162	2M140752928	IDD Fault	NA	IDD Fault	27	O	M	NA	p2597, Sol 159
163	2M140840681	GoldKlumpen2	EndOfTheRainbow	Rock	7	O	M	NA	p2597, Sol 159
163	2M140841136	GoldKlumpen4	EndOfTheRainbow	Rock	7	O	M	NA	p2597, Sol 159
163	2M140841645	GoldKlumpen7	EndOfTheRainbow	Rock	6	O	S	NA	p2597, Sol 159

Table A1. (continued)

Sol	Starting Image ID	Target	Feature	Target Type	No.	CS	S/M	Relation to RAT/MB	Pancam Sequence
163	2M140842057	GoldKlumpen1	EndOfTheRainbow	Rock	7	O	M	NA	p2597, Sol 159
164	2M140929646	Goldregen1	EndOfTheRainbow	Rock	8	O	S	NA	p2597, Sol 159
164	2M140930263	Goldregen2	EndOfTheRainbow	Rock	8	O	S	NA	p2597, Sol 159
164	2M140930743	Goldfin1	EndOfTheRainbow	Rock, Soil	8	O	S	NA	p2597, Sol 159
166	2M141109887	GoldBar1	FortKnox	Soil	6	O	S	Post-MB	None
166	2M141110586	Goldstaub	FortKnox	Soil	8	O	S	NA	p2545, Sol 180
167	2M141188588	Jaws	Goldfinger	Soil	6	O	S	NA	None
170	2M141460632	Fool's Gold	PotOfGold	Rock	7	O	M	NA	p2543, Sol 176
171	2M141551134	None	PotOfGold	Rock	10	O	S	NA	p2543, Sol 176
171	2M141552228	None	PotOfGold	Rock	20	O	S	NA	p2543, Sol 176
172	2M141639773	None	PotOfGold	Rock	1	O	M	NA	p2543, Sol 176
172	2M141640241	None	PotOfGold	Rock	1	O	M	NA	p2543, Sol 176
175	2M141896115	Wheat4	Breadbox	Rock	5	O	M	NA	p2530, Sol 166
175	2M141896655	Wheat1_tweaked	Breadbox	Rock	7	O	M	NA	p2530, Sol 166
175	2M141897363	Wheat2_tweaked	Breadbox	Rock	7	O	M	NA	p2530, Sol 166
175	2M141898060	Wheat3_tweaked	Breadbox	Rock	7	O	M	NA	p2530, Sol 166
177	2M142077070	Pearl1_tweaked	String_Of_Pearls	Soil	7	O	M	NA	p2541, Sol 177
177	2M142077752	Pearl1_stereo	String_Of_Pearls	Soil	7	O	M	NA	p2541, Sol 177
181	2M142429231	Shortbread1	CookieCutter	Soil	14	O	S	NA	p2544, Sol 180
191	2M143325094	Jerry	Loofah	Rock	8	O	S	NA	p2460, Sol 191
193	2M143498652	Mammoth4	Wooly Patch	Rock	12	O	S	NA	p2393, Sol 192
194	2M143587462	Sabre	Wooly Patch	Rock	34	O	S	Pre-RAT	p2393, Sol 192
196	2M143770387	Sabre	Wooly Patch	Rock	24	O	S	Post-RAT	p2556, Sol 200
197	2M143858480	Sabre Mastodon	Wooly Patch	Rock	12	O	S	Pre-RAT	p2393, Sol 192
199	2M144039937	Mastodon_real	Wooly Patch	Rock	13	O	S	Post-RAT,Post-MB	p2556, Sol 200
212	2M145185472	Cochiti	Clovis	Rock	6	O	S	NA	p2560, Sol 206
212	2M145185974	Jemez	Clovis	Rock	6	O	S	NA	p2560, Sol 206
212	2M145186552	Plano_spot	Clovis	Rock	24	O	S	Pre-Brush	p2560, Sol 206
214	2M145364683	Plano_spot	Clovis	Rock	24	O	S	Post-Brush	None
217	2M145630711	Plano_spot	Clovis	Rock	24	O	S	Post-RAT	p2569, Sol 226
225	2M146348689	None	Clovis	Rock	6	O	S	Post-Brush	p2569, Sol 226
227	2M146517433	Kilarney Flats	Frio	Soil	8	O	S	NA	None
228	2M146608749	Tiny Tim	Ebenezer	Rock	6	O	S	NA	p2571, Sol 227
228	2M146609432	Scrooge	Ebenezer	Rock	6	O	S	NA	p2571, Sol 227
228	2M146610135	Cratchit_2	Ebenezer	Rock	24	O	S	NA	p2571, Sol 227
229	2M146698436	Marley_tweaked	Ebenezer	Rock	6	O	S	NA	p2571, Sol 227
229	2M146698969	Fezziwig_tweaked	Ebenezer	Rock	6	O	S	NA	p2571, Sol 227
230	2M146785410	Cratchit_2(Ratchit_2)	Ebenezer	Rock	16	O	S	Post-Brush	p2583, Sol 237
232	2M146961183	Cratchit_2(Ratchit_2)	Ebenezer	Rock	24	O	S	Post-RAT	p2580, Sol 236
235	2M147232906	Fritz	Ebenezer	Rock	1	O	M	Post-MB	p2580, Sol 236
240	2M147676636	GreenEyes	Tikal_Area	Soil	24	O	S	Post-MB	p2597, Sol 263
240	2M147680383	Capture Magnet	Rover	Magnet	3	O	M	NA	p2113, Sol 240
240	2M147680697	Filter Magnet	Rover	Magnet	3	O	M	NA	p2113, Sol 240
258	2M149273525	Filter Magnet	Rover	Magnet	2	O	M	NA	p2113, Sol 258
258	2M149273739	Capture Magnet	Rover	Magnet	1	O	M	NA	p2113, Sol 258
258	2M149274486	GreenEyes	Conjunction Junction	Soil	24	O	S	Post-MB	p2597, Sol 263
259	2M149359510	Disturbance	Conjunction Junction	Soil	1	O	M	Post-MB	p2597, Sol 263
270	2M150337317	Best_Dwarf	Temples	Rock	6	O	S	NA	p2537, Sol 271
270	2M150337853	Dwarf_Edge2	Temples	Rock edge	6	O	S	NA	p2537, Sol 271
272	2M150518178	Mi_1	Tetl	Rock	32	O	S	NA	p2535, Sol 270
273	2M150604770	ThinLayer	Tetl	Rock	32	O	S	NA	p2535, Sol 270
276	2M150874294	Clump	Tetl	Rock	3	O	M	NA	p2535, Sol 270
276	2M150874704	Squeeze	Tetl	Rock	12	O	S	NA	p2535, Sol 270
276	2M150875892	Edge	Tetl	Rock	12	O	S	NA	p2535, Sol 270
279	2M151139145	Coffee	TakeAbreak	Soil	12	O	S	Pre-MB	p2540, Sol 280
281	2M151316310	Coffee	TakeAbreak	Soil	3	O	M	Post-MB	None
283	2M151494434	Koolik_2	Uchben	Rock	24	O	S	NA	p2543, Sol 293
286	2M151759502	Koolik_2	Uchben	Rock	24	O	S	Post-RAT	p2543, Sol 293
291	2M152203285	Chiikbes	Uchben	Rock	24	O	S	Post-Brush	None
292	2M152294327	Fine	Uchben	Rock	12	O	S	NA	p2543, Sol 293
297	2M152735759	Pickled	Lutefisk	Rock	24	O	S	NA	p2546, Sol 297
298	2M152823813	Flatfish	Lutefisk	Rock	6	O	S	Pre-Brush	p2546, Sol 297
298	2M152824173	Twins	Lutefisk	Rock	6	O	S	NA	p2546, Sol 297
298	2M152824576	Fish_eyes	Lutefisk	Rock	6	O	S	NA	p2546, Sol 297
298	2M152825154	RAT_Roe	Lutefisk	Rock	6	O	S	Pre-Brush	p2546, Sol 297
299	2M152912505	RAT_Roe	Lutefisk	Rock	12	O	S	Post-Brush	p2553, Sol 304
299	2M152915790	Ratfish	Lutefisk	Rock	12	O	S	Post-Brush	p2553, Sol 304
307	2M153619500	Capture Magnet	Rover	Magnet	3	O	M	NA	p2113, Sol 307
314	2M154240711	Tofurkey	Yams	Soil	16	O	S	NA	None
327	2M155394860	Tilted_Contact2	Solar Panel	Rover	12	O	M	NA	None
333	2M155927492	Chisel	Wishstone	Rock	6	O	M	Pre-Brush	p2563, Sol 332
333	2M155930269	Chisel	Wishstone	Rock	24	O	S	Post-Brush	p2563, Sol 332

Table A1. (continued)

Sol	Starting Image ID	Target	Feature	Target Type	No.	CS	S/M	Relation to RAT/MB	Pancam Sequence
334	2M156023978	Chisel	Wishstone	Rock	24	O	S	Post-RAT	p2569, Sol 337
341	2M156637750	Ds1	Penny	Soil	5	O	M	Post-APXS	p2573, Sol 343
348	2M157259088	Dreaming	Wishing Well	Rock	24	O	S	NA	None
350	2M157436854	Tilted_Contact2	Solar Panel	Rover	12	O	M	NA	p2266, Sol 356
352	2M157612888	RAT_Target	Champagne	Rock	24	O	S	Pre-Brush	None
352	2M157614502	Reachable_Lip	Champagne	Rock	6	O	S	Post-Brush	None
354	2M157792894	RAT_Target	Champagne	Rock	24	O	S	Post-Brush	None
358	2M158146856	RAT_Target	Champagne	Rock	24	O	S	Post-RAT	None
372	2M159392855	3x1_Tgt_2	Peace	Rock	18	O	S	Post-MB	p2543, Sol 381
372	2M159394037	2x2_mosaic	Peace	Rock	24	O	S	Post-MB	p2543, Sol 381
373	2M159478497	Equality	Peace	Rock	5	O	M	Post-MB	p2543, Sol 381
373	2M159478927	Equality_3	Peace	Rock	5	O	M	Post-MB	p2543, Sol 381
373	2M159479393	RAT_Justice	Peace	Rock	20	O	S	Post-MB	None
374	2M159567193	RAT_Justice	Peace	Rock	3	O	M	Pre-RAT	None
374	2M159572365	RAT_Justice	Peace	Rock	3	O	M	Post-RAT	p2543, Sol 381
376	2M159744609	RAT_Justice	Peace	Rock	16	O	S	Post-RAT	p2543, Sol 381
380	2M160099732	RAT_Justice	Peace	Rock	24	O	S	Post-RAT	p2543, Sol 381
380	2M160101370	RAT_Tailings	Peace	Rock	5	O	M	Post-RAT	p2543, Sol 381
380	2M160102005	Selma	Peace	Rock	20	O	M	NA	p2543, Sol 381
380	2M160105042	APXS_Target	Peace	Rock	5	O	M	Post-MB	p2543, Sol 381
386	2M160631523	Jambalaya	Alligator	Rock	4	O	S	Post-RAT	p2546, Sol 386
399	2M161789203	Marengo	Pasadena	Soil	5	O	M	Post-APXS	p2550, Sol 399
400	2M161877186	Paso Robles	Pasadena	Soil	24	O	S	Post-MB	p2551, Sol 400
415	2M163208054	Joker	Watchtower	Rock	5	O	M	Pre-Brush	p2273, Sol 413
415	2M163210479	Joker	Watchtower	Rock	20	O	S	Post-Brush	p2566, Sol 415
417	2M163384425	Joker	Watchtower	Rock	24	O	S	Post-RAT	p2574, Sol 419
419	2M163562003	Sky Flat	NA	Sky	1	C	M	NA	None
426	2M164185530	Big_clod	Paso_Robles2	Rock	7	O	M	NA	p2579, Sol 426
426	2M164186008	Bitty_clod	Paso_Robles2	Rock	7	O	M	NA	p2579, Sol 426
428	2M164353605	Paso_Dark_1	Paso_Robles2	Rock	24	O	S	Post-MB	p2530, Sol 431
428	2M164355316	Paso_Light_1	Paso_Robles2	Rock	24	O	S	Post-APXS	p2530, Sol 431
429	2M164448226	Bens_Clod	Paso_Robles2	Rock	7	O	S	Pre-Brush	None
429	2M164449658	Bens_Clod	Paso_Robles2	Rock	7	O	S	Post-Brush	p2592, Sol 429
431	2M164620111	None	Solar Panel	Rover	6	O	M	NA	None
431	2M164621116	Castoro	Paso_Robles2	Soil	5	O	M	NA	p2530, Sol 431
431	2M164630775	Paso_Dark_1	Paso_Robles2	Soil	4	O	M	Post-MB	p2530, Sol 431

[a]No., number of images in stack; CS, dust cover state (C, closed; O, open); S/M, stereo (S) or monoscopic (M) observation; Pancam Sequence, best multispectral observation of same target.

previously unseen characteristics in that whitish fines were exposed by the rover during instances of large wheel slip, similar to what was later observed further upslope on Husband Hill around Sol 400 [*Arvidson et al.*, 2006]. The MI observation of disturbed soil in a rover wheel track shown in Figure 26 appears to be a poorly sorted mixture of light-toned and darker materials. Due to operational constraints, no chemical measurements were made on this or similar targets at "Hank's Hollow." But morphologically and spectrally similar materials observed at the "Paso Robles" site around Sol 400 suggest a significant enrichment of sulfates which could be concentrated in the light-colored fraction of the soils and would be indicative of aqueous alteration in the West Spur/Columbia Hills province.

[104] Around solar conjunction, when commanding from Earth was not reliable and the usual operations process thus suspended (Sols 244-255), Spirit was stationed at a site between the West Spur and Husband Hill regions of the Columbia Hills. Probably due to the proximity of a topographic low, this site showed rocks and soils very similar to plains materials (S. Ruff et al., The rocks of Gusev crater as viewed by the Mini-TES instrument, manuscript in preparation, 2006), suggesting that this region actually is an outlier of the plains unit embaying the hills complex. An MI observation of the soil in front of the rover at the conjunction site is shown in Figure 27, acquired after being disturbed twice by the MB faceplate. The soil shows a texture similar to the plains soil that appears to be covered by accumulated airfall dust [*Herkenhoff et al.*, 2004b]. As on Sol 54, a clod of this surficial layer of dust (possibly indurated as a crust) adhered to the MB faceplate upon contact and was subsequently lifted from the underlying, relatively darker subsurface soil [*Yen et al.*, 2005]. Regions of the imprint where no clods were removed show that the dust layer was compressed by the MB contact with a very clear imprint of one of the MB faceplate attachment screw heads, suggestive of a significant fraction of silt- and clay-sized particles in the layer covering the darker subsurface soil.

[105] The disturbed soil at the Paso Robles site was analyzed on two occasions [*Arvidson et al.*, 2006], owing to its unique color characteristics, high albedo, and chemical composition (high SO_3 and P_2O_5). These observations are consistent with heavily altered materials having undergone aqueous processes resulting in soils dominated by ferric sulfates [*Ming et al.*, 2006]. MI images acquired of the altered soils (high albedo) and mixtures of this material with more typical soils (lower albedo), as well as the "Ben's Clod" rock after a RAT brushing operation, are shown in Figure 28. The compaction exhibited in the

lower albedo soils resulting from the Mössbauer imprint (Figure 28a) is better defined than that for the higher albedo soil (Figure 28b), indicative of less cohesion and less fine-grained material in the high-sulfate soils. The eroded nature of Ben's Clod after the RAT brushing (Figure 28c) provides evidence for the weakly cemented nature of this fragment.

6. Conclusions

[106] The data returned by Spirit's Microscopic Imager has provided key constraints in the interpretation of MER observations in Gusev crater. MI observations of plains rocks show olivine phenocrysts and evidence for secondary mineralization in vesicles and fractures. MI observations of rocks in the Columbia Hills are consistent with a volcaniclastic or impact origin, with evidence for case hardening in some cases. The poor sorting and abundance of angular grains observed in MI images imply that the Columbia Hills materials were deposited by a high-energy process, and that transport of the grains was very limited. Bedforms in Gusev crater are armored by coarse sand, while their interiors are much finer grained. Soils contain abundant dust grains and commonly show evidence of thin crusts that may be formed by recent evaporation of brines. Case hardening and submillimeter veins observed in the Columbia Hills rocks imply episodic subsurface aqueous fluid movement, which has altered multiple geologic units.

[107] The MI continues to acquire excellent data as the rover continues to explore Husband Hill. MI data acquired after Sol 450 will be described and interpreted in future publications.

Appendix A

[108] Targets observed by the MI were often also observed by Pancam and sometimes observed by the other IDD instruments as well. Table A1 summarizes MI observations during the first 540 sols of Spirit's mission and shows the relationship of each MI observation to RAT or Mössbauer (MB) observations of the same target. The far right column lists the sequence ID and sol of acquisition of Pancam observations of the same target. In some cases, the target was modified by the RAT or MB contact but not observed by Pancam after the modification; in these cases the entry is "None".

[109] **Acknowledgments.** We thank the MER rover planners for their outstanding support of Spirit IDD operations: Brian K. Cooper, Jeff Biesiadecki, Frank Hartman, Scott Maxwell, John Wright, Jeng Yen, Chris Leger, Robert Bonitz, Eric Baumgartner, Khaled Ali, Ashitey Trebi-Ollennu, and Mark Maimone. We also thank the NASA Ames support team: Matthew Deans, Laurence Edwards, Joel Hagen, Clayton Kunz, David Lees, Randy Sargent, Michael Wagner, and Anne Wright. Software tools developed at Cornell University by the Pancam team continue to be very useful in tracking and managing MI data products; we thank Elaina McCartney for her repeated assistance in operations planning. The MIPL MER team quickly generated many MI mosaics: Doug Alexander, Amy Chen, Oleg Pariser, Bob Deen, Jeff Hall, Mike Cayanan, Vadim Klochko, Elmain Martinez, and Charles Thompson. We also appreciate the support received from the MER team at the USGS in Flagstaff: Jeff Anderson, Tammy Becker, Devon Burr, Chris Isbell, Brian Lipkowitz, Dave MacKinnon, Janet Richie, Jac Shinaman, and Deborah Soltesz. Boris Semenov of JPL's Navigation and Ancillary Information Facility supported MI geometric processing by providing SPICE kernels in a timely fashion. Reviews by Bill Farrand, Aileen Yingst, Paul Geissler, and Laz Keszthelyi improved the quality of the manuscript and are much appreciated. This work was performed for the Jet Propulsion Laboratory, California Institute of Technology, sponsored by the National Aeronautics and Space Administration. The use of trade, product, or firm names in this paper does not imply endorsement by the U.S. Government.

References

Alexander, D., H. Mortensen, and R. Deen (2003), Mars Exploration Rover Project Software Interface Specification (SIS) Camera Experiment Data Record (EDR) and Reduced Data Record (RDR) operations data products, *JPL Doc. D-22846*, Jet Propul. Lab., Pasadena, Calif.

Alexander, D. A., et al. (2006), Processing of Mars Exploration Rover imagery for science and operations planning, *J. Geophys. Res.*, *111*, E02S02, doi:10.1029/2005JE002462.

Arvidson, R. E., et al. (2004), Localization and physical properties experiments conducted by Spirit at Gusev crater, *Science*, *305*, 821–824.

Arvidson, R. V., et al. (2006), Overview of the Spirit Mars Exploration Rover Mission to Gusev crater: Landing site to Backstay Rock in the Columbia Hills, *J. Geophys. Res.*, *111*, E02S01, doi:10.1029/2005JE002499.

Bell, J. (2004), MER 1 Mars Panoramic Camera EDR Ops, V1.0MER1-M-PANCAM-2-EDR-OPS-V1.0, NASA Planet. Data Syst., Washington, D. C.

Bell, J. F., III, et al. (2003), Mars Exploration Rover Athena Panoramic Camera (Pancam) investigation, *J. Geophys. Res.*, *108*(E12), 8063, doi:10.1029/2003JE002070.

Bell, J. F., III, et al. (2004), Pancam multispectral imaging results from the Spirit rover at Gusev crater, *Science*, *305*, 800–806.

Bell, J. F., III, J. Joseph, J. N. Sohl-Dickstein, H. M. Arneson, M. J. Johnson, M. T. Lemmon, and D. Savransky (2006), In-flight calibration and performance of the Mars Exploration Rover Panoramic Camera (Pancam) instruments, *J. Geophys. Res.*, *111*, E02S03, doi:10.1029/2005JE002444.

Bertelsen, P., et al. (2004), Magnetic properties experiments on the Mars Exploration Rover Spirit at Gusev crater, *Science*, *305*, 827–829.

Borg, L. E., L. E. Nyquist, Y. Reese, H. Wiesmann, C.-Y. Shih, M. Ivanova, and L. A. Taylor (2001), The age of Dhofar 019 and its relationship to other Martian meteorites, *Lunar Planet. Sci.* [CD-ROM], *32*, Abstract 1144.

Cabrol, N. A., J. D. Farmer, E. A. Grin, L. Richter, L. Soderblom, R. Li, K. Herkenhoff, G. A. Landis, and R. E. Arvidson (2006), Aqueous processes at Gusev crater inferred from physical properties of rocks and soils along the Spirit traverse, *J. Geophys. Res.*, doi:10.1029/2005JE002490, in press.

Campbell, S. W. (1999), Chemical weathering associated with tafoni at Papago Park, central Arizona, *Earth Surf. Processes Landforms*, *24*, 271–278.

Charola, A. E. (2000), Salts in the deterioration of porous materials: An overview, *J. Am. Inst. Conserv.*, *39*(3), 327–343.

Crisp, J. A., M. Adler, J. R. Matijevic, S. W. Squyres, R. E. Arvidson, and D. M. Kass (2003), Mars Exploration Rover mission, *J. Geophys. Res.*, *108*(E12), 8061, doi:10.1029/2002JE002038.

Danielson, G. E., P. N. Kupferman, T. V. Johnson, and L. A. Soderblom (1981), Radiometric performance of the Voyager cameras, *J. Geophys. Res.*, *86*(A10), 8683–8689.

Dorn, R. I. (2004), Case hardening, in *Encyclopedia of Geomorphology*, pp. 118–119, edited by A. S. Goudie, Routeledge, Boca Raton, Fla.

Farrand, W. H., J. F. Bell III, J. R. Johnson, S. W. Squyres, J. Soderblom, and D. W. Ming (2006), Spectral variability among rocks in visible and near-infrared multispectral Pancam data collected at Gusev crater: Examinations using spectral mixture analysis and related techniques, *J. Geophys. Res.*, *111*, E02S15, doi:10.1029/2005JE002495.

Gellert, R., et al. (2006), Alpha Particle X-Ray Spectrometer (APXS): Results from Gusev crater and calibration report, *J. Geophys. Res.*, *111*, E02S05, doi:10.1029/2005JE002555.

Gorevan, S. P., et al. (2003), Rock Abrasion Tool: Mars Exploration Rover mission, *J. Geophys. Res.*, *108*(E12), 8068, doi:10.1029/2003JE002061.

Goudie, A. S., and H. Viles (1997), *Salt Weathering Hazards*, John Wiley, Hoboken, N. J.

Grant, J. A., et al. (2004), Surficial deposits at Gusev crater along Spirit Rover traverses, *Science*, *305*, 807.

Greeley, R., et al. (2004), Wind-related processes detected by the Spirit Rover at Gusev crater, Mars, *Science*, *305*, 810.

Greeley, R., et al. (2006), Gusev crater: Wind-related features and processes observed by the Mars Exploration Rover Spirit, *J. Geophys. Res.*, *111*, E02S09, doi:10.1029/2005JE002491.

Hapke, B. (1993), *Theory of Reflectance and Emittance Spectroscopy*, 455 pp., Cambridge Univ. Press, New York.

Herkenhoff, K. (2004), MER 1 Mars Microscopic Imager EDR Ops V1.0, MER1-M-MI-2-EDR-OPS-V1.0, NASA Planet. Data Syst., Washington, D. C.

Herkenhoff, K. E., et al. (2003), Athena Microscopic Imager investigation, *J. Geophys. Res.*, *108*(E12), 8065, doi:10.1029/2003JE002076.

Herkenhoff, K., et al. (2004a), Mars Exploration Project Microscopic Imager Calibration Report, Rev. B. JPL D-19830, MER 420-6-704, Jet Propul. Lab., Pasadena, Calif.

Herkenhoff, K. E., et al. (2004b), Textures of the soils and rocks at Gusev crater from Spirit's Microscopic Imager, *Science*, *305*, 824.

Kirk, R. L. (1987), Part III. A fast finite-element algorithm for two-dimensional photoclinometry, Ph.D. thesis, pp. 165–258, Calif. Inst. of Technol., Pasadena.

Kirk, R. L., E. Howington-Kraus, B. Redding, D. Galuszka, T. M. Hare, B. A. Archinal, L. A. Soderblom, and J. M. Barrett (2003a), High-resolution topomapping of candidate MER landing sites with Mars Orbiter Camera narrow-angle images, *J. Geophys. Res.*, *108*(E12), 8088, doi:10.1029/2003JE002131.

Kirk, R. L., J. M. Barrett, and L. A. Soderblom (2003b), Photoclinometry made simple...?, paper presented at ISPRS-ET Working Group IV/9 Workshop Advances in Planetary Mapping, Int. Soc. for Photogramm. and Remote Sens., Houston, Tex.

Klingelhöfer, G., et al. (2003), Athena MIMOS II Mössbauer spectrometer investigation, *J. Geophys. Res.*, *108*(E12), 8067, doi:10.1029/2003JE002138.

Maki, J. (2004a), MER 1 Mars Hazard Avoidance Camera EDR Ops V1.0, NASA Planetary Data System, MER1-M-HAZCAM-2-EDR-OPS-V1.0, NASA Planet. Data Syst., Washington, D. C.

Maki, J. (2004b), MER 1 Mars Navigation Camera EDR OPS V1.0, MER1-M-NAVCAM-2-EDR-V1.0, NASA Planet. Data Syst., Washington, D. C.

Maki, J. N., J. J. Lorre, P. H. Smith, R. D. Brandt, and D. J. Steinwand (1999), The color of Mars: Spectrophotometric measurements at the Pathfinder landing site, *J. Geophys. Res.*, *104*, 8781–8794.

Maki, J. N., et al. (2003), Mars Exploration Rover Engineering Cameras, *J. Geophys. Res.*, *108*(E12), 8071, doi:10.1029/2003JE002077.

Martínez-Alonso, S., B. M. Jakosky, M. T. Mellon, and N. E. Putzig (2005), A volcanic interpretation of Gusev Crater surface materials from thermophysical, spectral, and morphological evidence, *J. Geophys. Res.*, *110*, E01003, doi:10.1029/2004JE002327.

McSween, H. Y., et al. (2004), Basaltic rocks analyzed by the Spirit Rover in Gusev crater, *Science*, *305*, 842–845.

McSween, H. Y., et al. (2006), Characterization and petrologic interpretation of olivine-rich basalts at Gusev crater, Mars, *J. Geophys. Res.*, *111*, E02S10, doi:10.1029/2005JE002477.

Ming, D. W., et al. (2006), Geochemical and mineralogical indicators for aqueous processes in the Columbia Hills of Gusev crater, Mars, *J. Geophys. Res.*, *111*, E02S12, doi:10.1029/2005JE002560.

Morris, R. V., et al. (2006), Mössbauer mineralogy of rock, soil, and dust at Gusev crater, Mars: Spirit's journey through weakly altered olivine basalt on the plains and pervasively altered basalt in the Columbia Hills, *J. Geophys. Res.*, doi:10.1029/2005JE002584, in press.

Nyquist, L. E., D. D. Bogard, C.-Y. Shih, A. Greshake, D. Stöffler, and O. Eugster (2001), Ages and geologic histories of Martian meteorites, *Space Sci. Rev.*, *96*, 105–164.

Pratt, W. K. (1978), *Digital Image Processing*, p. 72, Wiley-Interscience, Hoboken, N. J.

Reid, R. J., et al. (1999), Imager for Mars Pathfinder (IMP) image calibration, *J. Geophys. Res.*, *104*, 8907–8926.

Sargent, R., M. Deans, C. Kunz, M. H. Sims, and K. Herkenhoff (2005), The Ames MER Microscopic Image Toolkit, paper presented at IEEE Aerospace Conference, Big Sky, Mont., 5–12 March.

Squyres, S. W., et al. (2003), Athena Mars rover science investigation, *J. Geophys. Res.*, *108*(E12), 8062, doi:10.1029/2003JE002121.

Squyres, S. W., et al. (2004), The Spirit Rover's Athena science investigations at Gusev Crater, Mars, *Science*, *305*, 794.

Squyres, S. W., et al. (2006), Rocks of the Columbia Hills, *J. Geophys. Res.*, *111*, E02S11, doi:10.1029/2005JE002562.

Wang, A., et al. (2006a), Sulfate deposition in subsurface regolith in Gusev crater, Mars, *J. Geophys. Res.*, doi:10.1029/2005JE002513, in press.

Wang, A., et al. (2006b), Evidence of phyllosilicates in Wooly Patch, an altered rock encountered at West Spur, Columbia Hills, by the Spirit rover in Gusev crater, Mars, *J. Geophys. Res.*, *111*, E02S16, doi:10.1029/2005JE002516.

Yen, A. S., et al. (2005), An integrated view of the chemistry and mineralogy of Martian soils, *Nature*, *436*, 49–54.

R. Anderson, C. Budney, B. Franklin, C. Leff, J. N. Maki, R. Springer, and A. Yen, Jet Propulsion Laboratory, California Institute of Technology, 4800 Oak Grove Drive, Pasadena, CA 91109, USA.

B. A. Archinal, J. M. Barrett, K. J. Becker, M. G. Chapman, D. Cook, L. R. Gaddis, D. M. Galuszka, P. A. Garcia, T. M. Hare, K. E. Herkenhoff, E. Howington-Kraus, J. R. Johnson, R. L. Kirk, E. M. Lee, K. F. Mullins, B. L. Redding, M. R. Rosiek, L. A. Soderblom, R. M. Sucharski, T. Sucharski, and J. M. Torson, Astrogeology Team, U.S. Geological Survey, 2255 N. Gemini Drive, Flagstaff, AZ 86001, USA. (kherkenhoff@usgs.gov)

R. E. Arvidson, Department of Earth and Planetary Sciences, Washington University, Campus Box 1169, One Brookings Drive, St. Louis, MO 63130, USA.

J. F. Bell III, K. Kinch, S. W. Squyres, and R. Sullivan, Department of Astronomy, Space Sciences Bldg., Cornell University, Ithaca, NY 14853, USA.

N. A. Cabrol, NASA Ames Research Center/SETI Institute, Mail Stop 245-3, Moffett Field, CA 94035, USA.

B. L. Ehlmann, Environmental Change Institute, Department of Geography and Environment, University of Oxford, OX1 3QY, UK.

J. Farmer, Department of Geological Sciences, Arizona State University, P.O. Box 871404, Tempe, AZ 85287, USA.

S. Johnson, Department of Earth, Atmospheric and Planetary Sciences, Massachusetts Institute of Technology, Cambridge, MA 02139, USA.

M. Lemmon, Department of Atmospheric Sciences, Texas A&M University, 3150 TAMU, College Station, TX 77843, USA.

M. B. Madsen, Center for Planetary Science, Niels Bohr Institute for Astronomy, Physics and Geophysics, University of Copenhagen, DK-2100 Copenhagen, Denmark.

L. Richter, DLR Institut für Raumsimulation, Linder Hoehe, D-51170 Cologne, Germany.

M. H. Sims, NASA Ames Research Center, Mail Stop 269-3, Moffett Field, CA 94035, USA.

N. Spanovich, Lunar and Planetary Laboratory, University of Arizona, Tucson, AZ 85721, USA.